Materials Research Bulletin 176 (2024) 112803

Contents lists available at ScienceDirect

Materials Research Bulletin

journal homepage: www.elsevier.com/locate/matresbu

Review

Artificial synaptic devices based on biomimetic electrochemistry: A review

Ji Hyun Baek [a,1], In Hyuk Im [a,1], Eun-Mi Hur [b,c,d], Jungwon Park [e,f], Jongwoo Lim [g], Sangbum Kim [h], Kibum Kang [i], Soo Young Kim [j], Jae Yong Song [k,*], Ho Won Jang [a,l,*]

[a] Department of Materials Science and Engineering, Research Institute of Advanced Materials, Seoul National University, Seoul 08826, Republic of Korea
[b] Laboratory of Neuroscience, College of Veterinary Medicine, Seoul National University, Seoul, 08826, Republic of Korea
[c] Research Institute for Veterinary Science, College of Veterinary Medicine, Seoul National University, Seoul, 08826, Republic of Korea
[d] BK21 Four Future Veterinary Medicine Leading Education & Research Center, Seoul National University, Seoul 08826, Republic of Korea
[e] School of Chemical and Biological Engineering, Seoul National University, Seoul, 08826, Republic of Korea
[f] Center for Nanoparticle Research, Institute for Basic Science (IBS), Seoul National University, Seoul 08826, Republic of Korea
[g] Department of Chemistry, Seoul National University, 1 Gwanak-ro, Gwanak-gu, Seoul, 08826, Republic of Korea
[h] Department of Materials Science & Engineering, Inter-university Semiconductor Research Center, Research Institute of Advanced Materials, Seoul National University, Seoul, 08826, Republic of Korea
[i] Department of Materials Science and Engineering, Korea Advanced Institute of Science and Technology (KAIST), Daejeon, 34141, Republic of Korea
[j] Department of Materials Science and Engineering, Institute of Green Manufacturing Technology, Korea University, 145 Anam-ro, Seongbuk-gu, Seoul, 02841, Republic of Korea
[k] Department of Semiconductor Engineering, Pohang University of Science and Technology, Pohang, Gyeongbuk, 37673, Republic of Korea
[l] Advanced Institute of Convergence Technology, Seoul National University, Suwon, 16229, Republic of Korea

ARTICLE INFO

Keywords:
Artificial synapse
Synaptic transistor
Eletrochemical
Ionic synapse
ECRAM

ABSTRACT

The demand for advanced neuromorphic systems has surged due to their potential in artificial intelligence, robotics, and brain-computer interfaces. Artificial synapses are core elements in implementing hardware neuromorphic systems. Within the diverse realm of synaptic devices, electrochemical iontronic synapses (EISs) have gained prominence in recent years. EIS devices closely replicate natural synaptic mechanisms by precisely regulating ion concentrations within active regions, reversibly modulating conductivity based on the local perturbation of the electronic structure. EISs, guided by biomimetic electrochemistry, provide unique advantages such as precise weight modulation, consistent performance, low energy consumption, and rapid switching. Their adaptability to various ions and materials solidifies their applicability as neural network accelerators. In this review, we comprehensively explore EIS devices, examining their fundamental principles, recent progress, and forthcoming challenges. EISs hold the potential to bridge the gap between artificial and biological neural networks, offering a pathway to advanced hardware networks.

1. Introduction

Demand for advanced neuromorphic systems capable of emulating the intricate functionality of biological neural networks has risen in recent years, driven by the expanding horizons of artificial intelligence, robotics, and brain-computer interfaces [1–5]. This surge reflects our collective ambition to engineer machines that can not only process information with human-like efficiency but also demonstrate cognitive abilities such as learning, adaptation, and complex decision-making [6–8]. At the heart of the pursuit of such neuromorphic systems are synaptic devices, the core elements that enable communication and computation within neural networks. These artificial synapses serve as hardware platforms for neural networks that can learn, remember, and generalize from data through deep learning algorithms [9–12]. The study of synaptic devices, driven by multidisciplinary efforts in materials science, electronics, and neuroscience, has resulted in a diverse array of technological approaches [13–18]. The study of synaptic devices, driven by multidisciplinary efforts in materials science, electronics, and neuroscience, has resulted in a diverse array of technological approaches [13–21].

While a variety of synaptic devices have emerged, several notable categories stand out, each characterized by distinct advantages and

* Corresponding authors.
E-mail addresses: songjae3@postech.ac.kr (J.Y. Song), hwjang@snu.ac.kr (H.W. Jang).
[1] These authors contributed equally to this work.

https://doi.org/10.1016/j.materresbull.2024.112803
Received 30 November 2023; Received in revised form 15 March 2024; Accepted 27 March 2024
Available online 30 March 2024

challenges. Resistive switching devices, exemplified by resistive random-access memory (ReRAM), primarily rely on the formation and dissolution of conductive filaments to modulate synaptic weights [22–25]. This strategy offers merits of scalability, low power consumption, and fast switching speeds. However, the stochastic nature of filament formation can pose challenges in achieving precise control over synaptic weights, potentially leading to variations in performance [26–28]. Phase change memory (PCM), on the other hand, employs reversible phase transitions in materials, especially chalcogenides, to regulate synaptic efficacy [29–32]. PCM devices are renowned for their non-volatility, high endurance, and excellent scalability. Nevertheless, they are limited by relatively slower switching speeds and high power consumption, which may hinder their suitability for certain neuromorphic applications [33–35]. Another intriguing topic of research focuses on artificial synapse devices utilizing ferroelectric materials [36–39]. These devices leverage the inherent properties of ferroelectricity to enable rapid and low-energy switching. They hold promise for achieving efficient synaptic operations while maintaining stability and endurance. However, challenges related to integration into complex neuromorphic circuits and the need for innovative fabrication techniques remain areas of active investigation [24].

Within this landscape of artificial synapses, there has been a notable upsurge of interest in electrochemical iontroic synapses (EIS), which replicate synaptic plasticity mechanisms most akin to biological synapses found in the human brain [40–42]. The merits of these emerging devices lie in their ability to closely replicate the natural electrochemical iontronic processes governing signal transmission in biological neural systems [43]. EIS can finely tune synaptic weights by precisely controlling the concentrations of specific ions within the active weight control regions via biomimetic electrochemical reactions. Ions inserted into or extracted from a weight control layer modulate the channel conductivity via local perturbation of the electronic structure. This is similar to the static dopants in conventional semiconductors, but allows the dopant concentration to be changed in a more dynamic and reversible manner. Hence, the achieved synaptic modulation exhibits remarkable versatility, encompassing tiny and gradual increments appropriate for analog computing to huge and abrupt modifications required for dynamically programmable adaptive elements. Furthermore, the mechanism of synaptic plasticity in EIS closely resembles the fundamental processes observed at biological synapses where synaptic efficacy depends on the amount of neurotransmitters present in synaptic gap for signal transmission [44]. As a result, EIS holds the potential to bridge the gap between artificial and biological neural networks, offering a promising avenue for advancing hardware neural networks.

Furthermore, numerous research endeavors have been dedicated to the development of reliable and versatile artificial synaptic architectures through the employment of low-dimensional materials, such as one-dimensional nanowire channels and two-dimensional layered structures [45–48]. The exploration into nanostructured synaptic devices has been rigorously pursued with the objective of augmenting the integration density of these devices on semiconductor chips. Recent advancements in nanowire-based synaptic devices have facilitated reductions in device scale and the achievement of low-powering operation [49]. Additionally, two-dimensional materials, including graphene, transition metal dichalcogenides, black phosphorus, hexagonal boron nitride, and MXenes, have been recognized for their ability to form defect-free and atomically thin layers within two-dimensional van der Waals heterostructures [50]. This attribute significantly mitigates lattice mismatch and diminishes short-channel effects, thus enabling the realization of miniaturized device architectures. The recent utilization of these materials has underscored their distinctive structural, mechanical, electrical, and optical properties, which are pivotal for the advancement of photonic synapses [51]. Nevertheless, the imperative for ongoing exploration into novel device architectures remains paramount.

EIS devices present unique properties characterized by precise and deterministic weight modulation, consistent and reproducible performance, low energy consumption, and swift switching capabilities. EIS can finely tune synaptic weights by precisely controlling the concentrations of specific ions within the active weight control regions via biomimetic electrochemical reactions. Ions inserted into or extracted from a weight control layer modulate the channel conductivity via local perturbation of the electronic structure. Fig. 1 depicts EISs leveraging four types of cation covered in this review. Their adaptability to a wide spectrum of ions and material systems, encompassing species such as H^+, Li^+, and Na^+, gives the versatility to satisfy specific application requirements. Moreover, their application in crossbar array configurations makes them strong candidates for artificial neural network accelerators and the broader landscape of expanded neuromorphic systems. Continuing research efforts are progressively improving their linearity and symmetricity, heralding the emergence of a novel paradigm for energy-efficient neuromorphic computing [52,53].

In this review, we provide a comprehensive overview of the state-of-the-art artificial ionic synapses based on biomimetic electrochemistry. We explore various ion and material systems used in EIS devices, highlighting their fundamental principles, recent progress, and remaining challenges. Looking ahead, these advancements in EIS promise to enhance neuromorphic computing, offering increased efficiency and sophistication.

2. Artificial synapses and synaptic behaviors

In the nervous system, synapses serve as junctions that enable fast, point-to-point information transfer not only between two neurons in the brain, but also from neurons in the brain to other cells in the periphery [54,55]. This transmission occurs when an electrical signal is generated in the form of an action potential or a receptor potential in the presynaptic neuron. This change in membrane potential triggers presynaptic exocytosis and the subsequent release of neurotransmitters into the synaptic cleft. In the realm of neuromorphic computing, artificial synapses are designed to mimic the functionality of biological synapses. Artificial synapses must fulfill certain fundamental criteria to effectively emulate their biological counterparts. These criteria encompass analog resistance modulation, regulation of synaptic weights, and the ability to implement practical synaptic plasticity mechanisms. Within synaptic devices, the device resistance correspond to synaptic weights signifying the strength of the connection between neurons. Consequently, the resistance states of the device should exhibit gradual and multi-state adjustability.

Synaptic plasticity refers to the activity-dependent modifications of the strength or efficacy of synaptic transmission [56,57]. There are two principal directions in synaptic weight changes: potentiation and depression. Potentiation denotes an augmentation of synaptic weight, resulting in increased conductance, while depression signifies a reduction in synaptic weight, leading to decreased conductance. These processes encompass short-term and long-term modulations. The short-term potentiation (STP) and short-term depression (STD) manifest as a transient enhancement and degradation in synaptic weight in response to relatively sparse input pulses, which then promptly reverts to its initial state [58]. Conversely, repetitive or tetanic stimulation of synapses with prolonged trains of stimulation applied at hight frequencies results in sustained strengthening and weakening of synaptic connections, respectively referred to as long-term potentiation (LTP) and long-term depression (LTD) [59]. Fig. 2a and b display STP and LTP characteristics in artificial synaptic devices, respectively. These dynamic alterations in synaptic weight facilitate information storage and processing within neuromorphic systems. Furthermore, a diverse range of synaptic plasticities, which respond to varying input signal patterns, are extensively investigated as major synaptic phenomena. Fig. 2c–h present the basic synaptic modulations. Fig. 2c illustrates the characteristics of spiking-rate-dependent plasticity (SRDP), where the rate of weight alteration rapidly increases with higher frequencies of the weight modulation spike. The spike-voltage-dependent plasticity (SVDP)

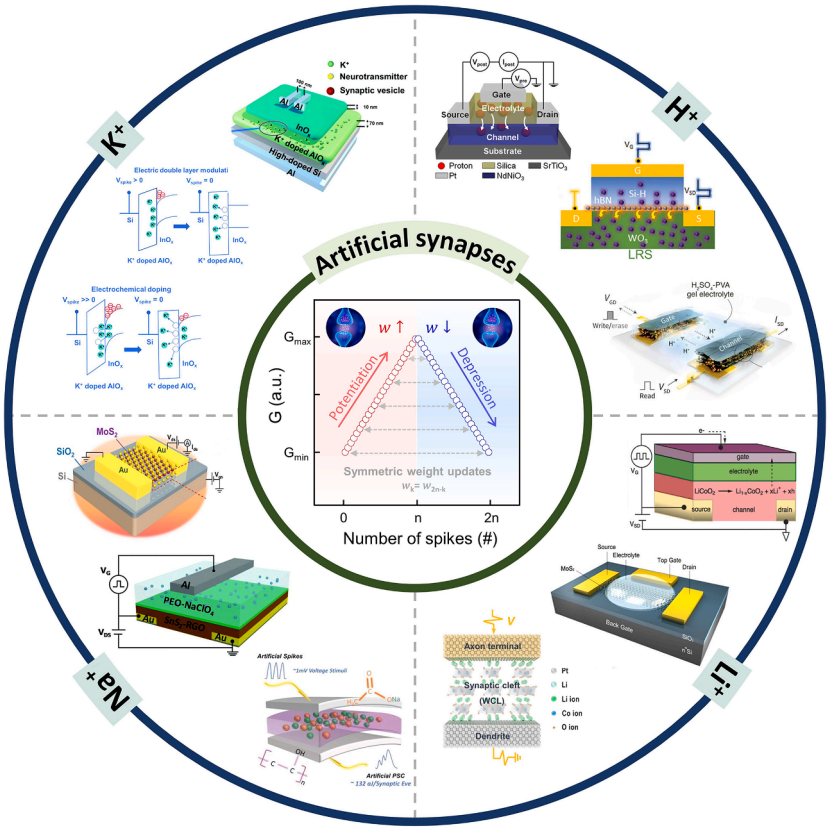

Fig. 1. Artificial synaptic devices leveraging the electrochemical reaction of various cations.

depicted in Fig. 2d demonstrates that the magnitude of the unit weight grows as the amplitude of the input spike increases. The spiking-number-dependent plasticity (SNDP) in Fig. 2e reveals that the dynamic range varies in accordance with the number of weight modulations. Here, a trade-off relationship between dynamic range and linearity is observed. Similar to the SVDP characteristic, the spiking-width-dependent plasticity (SWDP) shown in Fig. 2f exhibits that the unit weight change step incrementally rises with prolonged durations of the input spike. Fig. 2g depicts paired-pulse facilitation (PPF), a form of STP wherein the synaptic response is potentiated when two stimuli are administered sequentially. Fig. 2h illustrates spike-timing-dependent plasticity (STDP), a synaptic modulation which dynamically adjusts synaptic efficacy according to the temporal correlation between pre- and postsynaptic spikes.

Along with these synaptic behaviors, artificial synaptic devices must function in a reliable analog manner as essential hardware components for neuromorphic computing [15]. The linearity and symmetry of weight updates are paramount in determining the computational performance of neuromorphic systems. Even though the requirements are not as strict as those for typical memory devices, synaptic devices must still demonstrate adequate resolution in dynamic range and on/off ratio to effectively execute multi-bit functions. Furthermore, long-term retention of programmed conductance states without degradation during the computation period is a fundamental requirement. In addition, neuromorphic computing strives to be an energy-efficient technology, characterized by low-power operation and highly parallel matrix computing [60,61]. Consequently, low operating power stands as one of the principal criteria for assessing synaptic devices.

3. Proton-based EISs

Protons, which are hydrogen cations, are small and have a rapid diffusion rate within insulator matrices [62]. They possess the smallest ionic radius, with a Shannon-Prewitt effective ionic radius of approximately −0.18 Å when two-fold coordinated and −0.38 Å when one-fold coordinated [63]. This small size makes them ideal for achieving high modulation speed, low energy consumption, and enhanced endurance in electronic devices [64,65]. Over the past decade, various approaches involving alkali metal ions like Li^+, Na^+, and K^+ have been explored [52,53]. Among these, electrochemical proton-based devices offer an advantage by minimizing contamination issues during the fabrication process. Consequently, proton intercalation devices have an edge in scalable programmable resistors due to their compatibility with the complementary metal-oxide semiconductor (CMOS) technology [66,67].

The utilization of proton intercalation within an inorganic WO_3 film enabled the emulation of synaptic characteristics with benefits such as low energy consumption, long retention, and improved symmetry [68]. WO_3 can be a promising host material for proton intercalation due to its ability to transition from an undoped insulating state ($E_g = 2.8{\sim}3.2$ eV) [69] to a protonated metallic state, as well as its compatibility with Si processes. Yao et al. propoesed three-terminal EIS based on proton intercalation in a WO_3 film [66]. Fig. 3a illustrates the configuration of protonic EISs where the channel area is occupied by a monoclinic WO_3 film, and a proton electrolyte layer, Nafion-117, is applied through spin-coating. The palladium hydride (PdH_x) gate electrode serves as a proton conductor layer. The conductance ($G = I_d/V_{ds}$), which represents the strength of the synapse, is measured between the source and drain electrodes. The application of the current pulse to the gate (I_G) drives protons into or out of the WO_3 channel area. When a positive gate pulse is applied, PdH_x is electrochemically oxidized, releasing protons into the Nafion electrolyte. The protons then migrate to the WO_3 layer due to the driving force of the gate voltage (V_G). Upon reaching the channel area, proton intercalation occurs, resulting in H_xWO_3. The conductivity of H_xWO_3 varies based on proton concentration, as depicted in Fig. 3b. The deprotonation process occurs in reverse when negative I_G is applied to

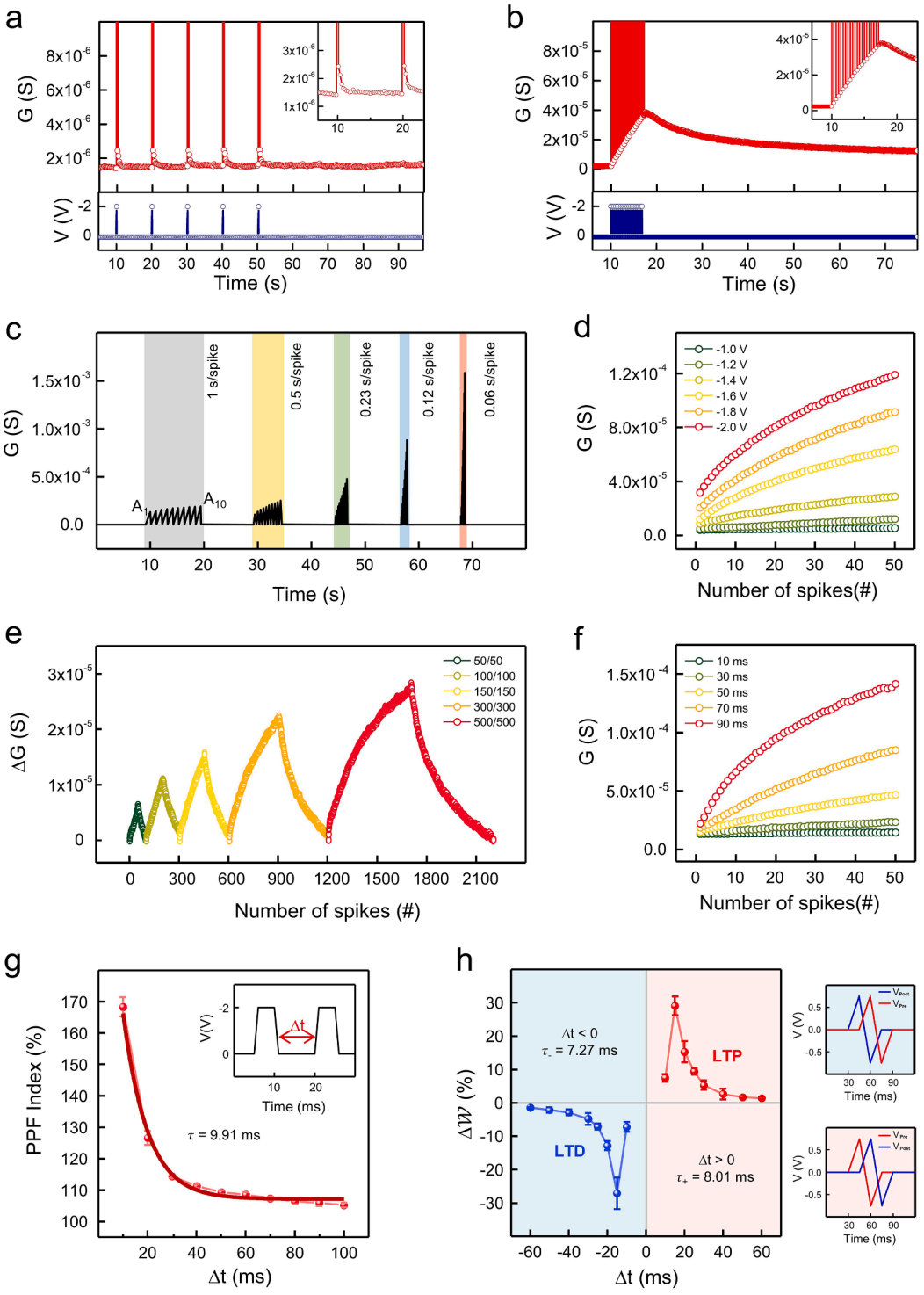

Fig. 2. Synaptic plasticity and basic synaptic behaviors in artificial synaptic devices. Basic synaptic modulations in EIS devices including (a) Short-term potentiation (STP), (b) Long-term potentiation (LTP), (c) Spiking-rate-dependent plasticity (SRDP), (d) Spiking-voltage-dependent plasticity (SVDP), (e) Spiking-number-dependent plasticity (SNDP), (f) Spiking-width-dependent plasticity (SWDP), (g) Paired-pulse facilitation (PPF), and (h) Spiking-timing-dependent plasticity (STDP). Reproduced with permission. [92] Copyright 2023, Springer Nature.

the gate. The slope of the conductivity change exhibits three aspects: a low conductance regime, a medium conductance regime, and a high conductance regime. Fig. 3c and d illustrate the potentiation (protonation) and depression (deprotonation) behavior in the low and high conductance regimes, respectively. Lower proton content results in better symmetry and a higher ratio of maximum to minimum conductance (G_{max}/G_{min}). Additionally, shallower potentiation and depression ranges provide improved symmetry, although this reduces the G_{max}/G_{min} ratio.

To address the challenge of the absence of a CMOS-compatible all-solid-state electrolyte, a nanoporous phosphosilicate glass (PSG) solid electrolyte was proposed by Alamo's group [70]. Solid electrolytes based on organic materials are susceptible to chemical and thermal instability during CMOS fabrication procedures [71]. In Fig. 3e, a

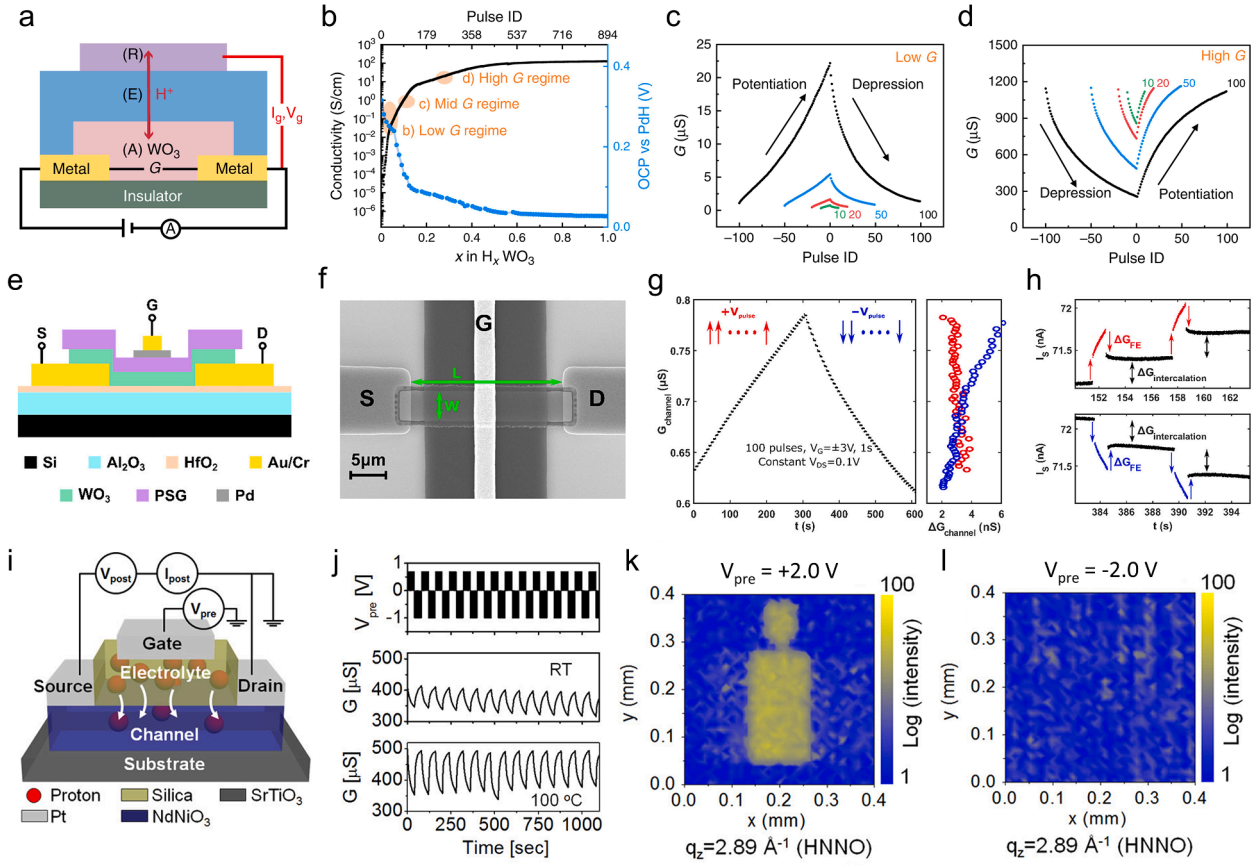

Fig. 3. Electrochemical synaptic transistors based on proton intercalation. (a) The configuration of source-drain-gate in a three-terminal synaptic transistor based on proton intercalation in the WO_3 channel. (b) Protonation dependence of WO_3 conductivity. Reversible conductance change with symmetry in (c) low conductance regime and (d) high conductance regime. Reproduced with permission. [66] Copyright 2020, Springer Nature. (e) Schematic and (f) top-view SEM image of the ion intercalation-based programmable resistors. (g) Increases and decreases in conductance upon 100 positive voltage pulses followed by 100 negative voltage pulses. (h) Conductance change by the programming pulses, collaborating a volatile field-effect conductance fluctuation and a nonvolatile intercalation-induced conductance modulation. Reproduced with permission. [70] Copyright 2021, American Chemical Society. (i) Schematic device architecture of $NdNiO_3$-based synaptic transistor. (j) Synaptic behaviors in $NdNiO_3$-based synaptic transistor at room temperature and 100 °C. Spatially resolved synchrotron X-ray microdiffraction mappings of hydrogen (k) after initial +2 V pulse for hydrogen injection and (l) after subsequent −2 V pulse for hydrogen rejection. Reproduced with permission. [73] Copyright 2019, American Chemical Society.

three-terminal EIS with a WO_3 channel, a PSG electrolyte layer, and a Pd gate reservoir demonstrates a fully CMOS-compatible process flow. Fig. 3f displays a top-view scanning electron microscope (SEM) image of a protonic programmable resistor with a WO_3 channel area measuring 5 μm in width and 25 μm in length. Similar to previous work, the protonation mechanism involves the ejection of protons from the gate reservoir as PdH_x, diffusion through the PSG electrolyte, and intercalation into the WO_3 channel area. Fig. 3g displays the highly symmetric conductance modulation behavior in a protonic programmable resistor, attributable to the high proton conductivity and electron-insulating property of the PSG electrolyte. Conductance increases with 100 positive voltage pulses and decreases with subsequent 100 negative pulses. The increase in conductance is identical to the decrease, resulting in a high degree of symmetry. The detailed conductance modulation is depicted in Fig. 3h. The source current (I_S) steps up or down with the application of positive or negative gate pulses. Upon applying the gate pulse, there is a sudden increase or decrease in channel conductance. After the gate pulse is removed, Is relaxes to a higher or lower conductance level than the previous state. The conductance change comprises both nonvolatile and volatile modulation.

Although reliable performance in preceding protonic intercalation synapses, high energy consumption has been required due to the wide bandgap oxide of the channel layer [72]. To develop low-power EISs, a metal-insulator transition (MIT) material was proposed as the channel matrix by Oh et al. [73]. Fig. 3i presents the EIS transistor fabricated with porous silica electrolyte and a correlated oxide $NdNiO_3$ channel grown on (001)-oriented $SrTiO_3$ substrate. The porous sol-gel silica electrolyte absorbs water vapor from the ambient atmosphere and water is electrolyzed into protons and hydroxyl molecules when a potential is applied from the gate electrode. This potential drives proton movement through the electrolyte and protonation into the $NdNiO_3$ channel. As a result, the Ni^{3+} ion in the metallic $NdNiO_3$ oxide is transformed into a correlated Ni^{2+} ion, which exhibits an insulating status. As shown in Fig. 3j, the positive gate pulse train modulates the conductance to a low conductance state due to the metal-insulator transition prompted by proton intercalation. Conversely, the initialization of the $NdNiO_3$ channel, achieved by deprotonation with a negative pulse train, results in increased conductance. Spatially resolved synchrotron X-ray microdiffraction mappings in Fig. 3k and l prove that the protonation and deprotonation in the $NdNiO_3$ channel depend on the polarity of gate potential. When a positive V_G (+2 V) is applied, the local intensity of the Bragg diffraction for H—$NdNiO_3$ (q_z = 2.89 $Å^{-1}$) suddenly rises, as depicted by a yellow signal in Fig. 3k. However, after subsequent negative V_G (−2 V) application, the signal decreases due to the hydrogen rejection.

Hwang's group introduced hexagonal boron nitride (hBN) single-layers as a proton transport matrix to enhance memory state-retention and cycling stability [74]. This improved EIS transistor, based on

proton transport through hBN, is illustrated in Fig. 4a. The device features a vertical stack with single-layer hBN sandwiched between a WO_3 channel and a Si-H reservoir. In the initial state, with no net proton migration, the device exhibits a native high conductance state. When a positive V_G is applied, protons are transported from the Si-H reservoir to the WO_3 layer. Single-layer hBN, known for its high polarity, provides a negatively charged electron cloud during the transport of small cations, facilitating their movement. This results in a phase transition in the channel area to H_xWO_3 through protonation, leading to a low conductance state in the device. Fig. 4b depicts analog conductance modulation behavior with high linearity and symmetry. In Fig. 4c, the programmed states are maintained with long retention, enabling both LTP and LTD modulation. The hBN-protonic intercalation EISs show a uniform distribution during weight updates in potentiation cycling and depression cycling, as demonstrated in Fig. 4d. Furthermore, in Fig. 4e, the EISs exhibit excellent endurance up to 58,400 pulses. A multilevel cell (MLC) neural network was simulated using the potentiation and depression data to validate its potential in pattern recognition. In the learning simulation, 528 input neurons process MNIST input images of 24 × 22 pixels. Each neuron is connected to one pixel of the image. At each training epoch, the MLC is trained with 20,000 patterns. As shown in Fig. 4f, the hBN-protonic intercalation EISs achieved an accuracy of 93.27 % after 20 epochs, which is comparable to the case using an ideal synapse with 95.71 % accuracy.

Polymer-based intercalation devices have demonstrated sub-microsecond switching speeds but were limited by their incompatibility with the semiconductor industry. For suitable on-chip fabrication in Si electronics, similar to 2D materials, polymer-based intercalation materials need to provide integration stability [40,71]. Therefore, 2D titanium carbide ($Ti_3C_2T_x$) MXene was employed by Melians et al. for high-performance intercalation devices compatible with Si fabrication processes [75]. As shown in Fig. 4g, multilayered $Ti_3C_2T_x$ MXene, fabricated via layer-by-layer (LbL) self-assembly, serves as the active layer for the electrochemical reaction of protons from PVA-H_2SO_4 electrolyte. The incorporation of tris(3-aminopropyl)amine (TAPA) spacer between MXene bilayers reduces electronic conductivity and enhances ionic access to the redox-active sites. The $(MXene/TAPA)_n$ intercalation EIS exhibits lower power consumption and faster switching. A $(MXene/TAPA)_6$ intercalation EIS capable of implementing synaptic potentiation and depression over 108 cycles showcased high endurance, as diaplaued in Fig. 4h. With the switching statistics, an artificial neural network (ANN) simulation for image classification of 28 × 28-pixel handwritten digits was conducted in Fig. 4i. The $(MXene/TAPA)_6$ intercalation synapse achieves a 90 % accuracy rate, significantly outperforming conventional resistive switching-based synapse devices.

4. Li^+-based EISs

Along with protons, Li-ions are one of the most commonly employed elements in EIS devices [76,77]. Numerous early EIS devices relied on the migration of Li-ions within materials initially designed for secondary Li-ion battery (LIB) applications. Li-ion, being the second smallest ion, exhibits facile migration within solids, which holds promise for devising devices with swift synaptic modulation capabilities as well as minimal energy consumption [78,79]. Additionally, materials characterized by high Li-ion mobility have undergone extensive research in the realm of battery applications, serving as a valuable foundation for material selection in the development of EIS devices [80–82].

Talin's group first reported a Li-ion synaptic transistor for analog computation (LISTA) in 2017 [41]. The SEM image of Fig. 5a shows LISTA which represents an all-solid-state, nonvolatile redox transistor featuring a resistance change capabilities that rely on the intercalation of Li-ion within a $Li_{1-x}CoO_2$ channel. In the LISTA device, the V_G regulates the Li content within the channel as shown in Fig. 5b. The application of a negative V_G relative to the open circuit potential drives the electrochemical migration of Li-ions from the $Li_{1-x}CoO_2$ channel into the gate electrode via lithium phosphorous oxynitride electrolyte (LiPON) solid electrolyte. The extraction of Li ions induces the oxidation of Co-ions from a valence state of 3^+ to 4^+, resulting in the generation of positively charged polarons. As the Li fraction in $Li_{1-x}CoO_2$ diminishes to 0.5, there is an approximately six-fold increase in the electronic conductivity of the channel, leading to a transition from an insulating to a metallic state. This transition is distinguished by its remarkable reversibility, wherein the application of a positive voltage V_G enables the reinsertion of Li-ions into the channel, thereby restoring it to its initial conductivity. This mechanism is akin to the charging process observed in LIBs, where the charge/discharge redox reactions are promoted by an external current source. In the charging stage illustrated in Fig. 5c with a negative I_G, the source-drain conductance (G_{SD}) experiences a notable increase from 4.5 to 270 μS, concurrently shifting the open circuit potential (OCP) from 0 to −4.2 V. Subsequently, a positive I_G is applied, discharging the device to nearly 0 V and restoring it to a low conductance state. Fig. 5d displays a $G_{SD}(t)$ plot during a current-controlled operation where the pulse train induces a gradual rise in $G_{SD}(t)$ from 257 to 266 μS. For each "write" operation with finite I_G, there is an observable gradient in the recorded channel conductance, attributable to the extraction of Li-ions from the channel, whereas the $G_{SD}(t)$ remains constant during the "read" operation. Fig. 5e illustrates the alteration in conductance, denoted as ΔG, resulting from a current-controlled "write" operation ($|I_G| = 200$ nA). The data is plotted against the initial conductance state, referred to as G_0, for both potentiation and depression. The probability distribution plots exhibit remarkable linearity and feature a narrow distribution centered around a single value of the mean change in conductance across the entire spectrum of G_0. The linear relationship depicted in Fig. 5f suggests that the LISTA system is proportional to the quantity of charge transferred, related to the pulse amplitude and the pulse duration. These linear tendencies enable estimating an exceptionally low level of energy dissipation in LISTA, which amounts to less than 10 aJ per "write" operation.

Likewise, Yang et al. demonstrated an all-solid-state and three-terminal EIS transistor based on a 2D α-MoO_3 channel [83]. Li-ions serve as dopants contributing free electrons to MoO_3, being injected or extracted into the channel under the applied electric field, thereby changing the channel conductance as illustrated in Fig. 5g and h. Fig. 5i shows that the strengthening of excitatory postsynaptic current (EPSC) in proportion to the amplitude of V_G, which governs the quantity of doped Li-ions. A volatile stage was observed before nonvolatile weight modulation, as Li-ions that had temporarily accumulated at the electrolyte and channel interface immediately after voltage application were soon dispersed. The EPSC cahnge characterized by the volatile and nonvolatile aspects are depicted in Fig. 5j. The ratio of volatile and nonvolatile modulations is contingent on the amplitude and duration of the weight control voltage pulse. As displayed in Fig. 5k, iterative weight adjustments led to gradual LTP and LTD modulations. Fig. 5i illustrates the essential multi-state characteristics of LTP and LTD, which are crucial for implementing analog neuromorphic computational functions. The iterative weight updates through voltage pulses are shown in Fig. 5m, each cycle providing 50 synaptic potentiaion and depression. Indeed, linearity and symmetry in weight updates play key roles in determining the learning accuracy of neuromorphic computing systems. Enhancing the ionic capacity of the channel material and the sensitivity to doping, thereby increasing the conductivity change rate, can lead to a substantial improvement in the linearity of synaptic transistors. Deliberate regulation of ion implantation can effectively mitigate conductance saturation and contribute to improved linearity, albeit at the cost of reducing the dynamic range.

2D materials with structures favorable to ionic intercalation are being explored as potential channel materials of EISs [84,85]. Zhu et al. reported an EIS transistor based on Li-ion intercalation into 2D WSe_2 channel [86]. Fig. 6a depicts ionic-gated synaptic transistors based on van der Waals layered crystal with a polymer electrolyte containing

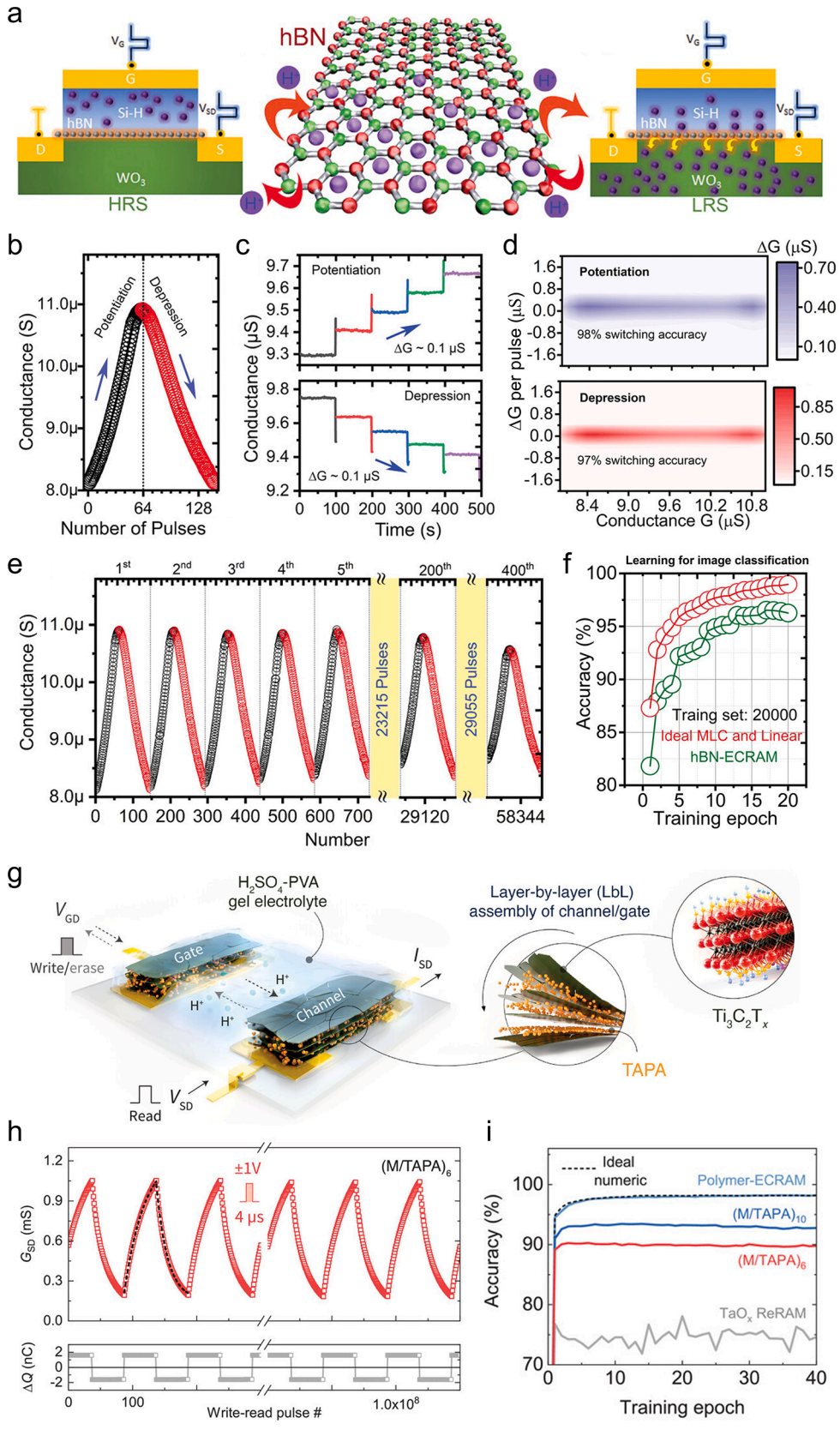

(caption on next page)

Fig. 4. Synaptic devices based on proton diffusion into 2D active channel. (a) Analog switching mechanism in hBN-ECRAM synapses based on proton diffusion through single-layer hBN and alteration of the proton concentration in the ion-sensitive channel. (b) Potentiation and depression behaviors in hBN-ECRAM synapse by applying 146 write and erase pulses. (c) Nonvolatility in the synaptic devices displaying the retention characteristics of multiple states. (d) Conductance distribution plots of 40 potentiation and depression cycles and their switching accuracy predicted by the number of training pulses. (e) Multiple cycles of potentiation and depression in the hBN-ECRAM synapse by 58,400 training pulses. (f) Image recognition accuracy of the hBN-ECRAM synapse compared to the ideal device. (g) Schematic of the architecture of Mxene/TAPA-based ECRAM device. Multilayer $Ti_3C_2T_x$ MXene films by LbL assembly stores inserted protons through the electrochemical reaction. (h) High endurance in $(Mxene/TAPA)_6$ ECRAM device over 10^8 write-read events. (i) Simulated ANN accuracy for image classification on 28 × 28-pixel handwritten digit. Reproduced with permission. [74,75] Copyright 2021, Wiley-VCH GmbH.

$LiClO_4$ dissolved in polyethylene oxide (PEO). In this configuration, Li-ions in the electrolyte can drive into or extract from layered transition metal dichalcogenides under certain gate biases, thereby generating ionic gating effects. The introduction of Li-ions into WSe_2 induces a shift in the material's Fermi level towards the conduction band, leading to an increase in channel conductance. Fig. 6b illustrates the two types of ionic gating processes that enable synaptic activities. When a gate bias is applied, Li-ions diffuse and adhere to the surface of the 2D material. If the gate bias is promptly removed, the adhered Li-ions diffuse back into the ion gel reversibly. This transient electrochemical reaction induced an instantaneous alteration in channel conductance, which was interpreted as STP behavior. However, if the application of gate bias is repeated for an extended duration, the absorbed Li-ions become intercalated into the van der Waals material. Consequently, even after the gate bias is removed, the spontaneous release of intercalated Li-ions into the ion gel is impeded, leading to LTP. Fig. 6c and d depict STP and LTP modulation, respectively. In STP, the strengthened currents are fully released back, while in LTP, some modulated channel resistance is maintained. The diverse time scales of synaptic activity are then dictated by how Li-ion is integrated into the channel material. Fig. 6e shows cross-sectional high-resolution transmission electron microscopy (HRTEM) images of the intact layered WSe_2 film after STP and LTP modulation. The structural disorder is only observed after the LTP modulation, indicating ion intercalation into the van der Waals gaps. The process of ion intercalation is further confirmed through selected area electron diffraction (SAED) analysis. Fig. 6f displays the SAED pattern of WSe_2 film during LTP, revealing an additional set of diffraction points. Notably, extra Li layers with a 2d spacing, depicted in Fig. 6g, can be observed alongside the existing d-spacing WSe_2 layers. The magnitude of long-term weight change, which is related to the amount of incorporated Li-ions, depends on the number of $_{WSe2}$ layers since Li-ion insertion occurs within the van der Waals gap. As shown in Fig. 6h, a substantial increase in Δw/w0 is evident in WSe_2 channels containing approximately 35 or more layers. The increased thickness of the channel layer likely offers additional sites for Li-ion intercalation and contributes to impeding the reverse diffusion of deeply intercalated ions, consequently leading to significant and long-term weight changes.

Bao and colleagues developed a double-gate neuristor based on a 2D MoS_2 channel that incorporates Li-ion intercalation, showcasing its potential in EIS and additional neuronal applications [87]. Fig. 6i illustrates a MoS_2-based neuristor featuring a dual-gated transistor configuration. The integration of both the top gate (TG) and the back gate (BG) facilitates the separation of an ionic gate and an electronic gate, enabling independent control over the ionic relaxation and electronic relaxation processes. The memory effects of the MoS_2 neuristor are attributed to a relaxation process of Li-ions. Thus, the MoS_2 neuristor functions as a synaptic transistor when the ionic TG is engaged. As illustrated in Fig. 6j, LTP characteristics can be emulated by impulsing several stimuli through the TG. Like the mechanism described above, Li-ions are intercalated into the van der Waals gaps of MoS_2 under strong stimulation and do not spontaneously escape, allowing the maintenance of high channel conductance. Fig. 6k presents the continuous modulation of channel conductance, demonstrating superior linearity and symmetry compared to conventional transition metal oxide-based artificial synapses. The saturation observed during the depression phase is attributed to spontaneous Li-ion desorption, which requires fewer stimulations to remove Li-ions from the MoS_2 channel. When the electronic BG is activated, the MoS_2 neuristor transforms into an n-type metal-oxide-semiconductor field-effect transistor. Significantly, the neuristors successfully replicate the integrate-and-fire function of a biological neuron through a combination of TG and BG operations. Throughout neuronal activity, a continuous bias voltage is applied to the drain electrode, and I_d is considered as the membrane current. In situations where the MoS_2 channel is undoped, the neuristor demonstrates a high threshold voltage, causing the clock applied to the BG to be insufficient to turn on the channel. Consequently, the high potential applied to the drain cannot propagate to the source. Fig. 6l and m illustrate the I_d response at V_A values of 0.5 V and 1.5 V, respectively. When weak input pulses are administered to the TG, the occurrence of firing spik is minimal. Conversely, stronger input pulses substantially elevate the probability of firing, ultimately achieving 100 %. Fig. 6n demonstrates the relationship between the number of output spikes in a 10 s interval and the amplitude of TG input. The capability to adjust the firing probability via input signal manipulation is well proved.

Taghi et al. reported an electrochemical graphene synapse which directly inspired by the structure and operational principles of LIBs [88]. Fig. 7a illustrates a graphene-based EIS consisting of a 2D graphene channel, a lithium phosphate (LFP) reference electrode, and a solid electrolyte ($LiClO_4$ in PEO). Graphene and LFP are commonly employed materials as anode and cathode in LIBs, respectively, where the charge and discharge processes involve the mutual movement of Li-ion ions across the electrolyte as shown in Fig. 7b. The electrical conductivity of the channel is reversibly programmed through signals from the LFP reference electrode, which regulates the Li-ion concentration between the graphene layers. The 2D structure of graphene provides an ideal environment for ion intercalation, allowing for stable and precise weight control. In Fig. 7c, the galvanostatic discharge measurement shows the Li fraction change of lithium-graphene compounds as the channel undergoes various intermediate phases during the progressive process of lithium-ion intercalation. Each intermediate state, starting from the initial stage LiC_{72} to the stoichiometric maximum LiC_6, exhibits an almost uniform distribution of lithium intercalants. Throughout the whole intercalation process, synaptic weights were increased by approximately 700 % as presented in Fig. 7d. Fig. 7e and f display synaptic potentiation and depression in 2D graphene EISs, respectively. The initial substantial change in channel conductance is attributed to a combination of the doping effect and the electric double layer (EDL) gating effect of the current pulse, which rapidly stabilizes into a long-term resistance change after the transient influence. In addition, reproducibility in weight modulation was demonstrated by achieving equivalent conductance changes in both potentiation and depression, based on highly reversible processes of Li-ion intercalation and deintercalation. Therefore, as depicted in Fig. 7g, liniear and symmetric weight updates for LTP and LTD across 250 distinct states can be achived with an energy consumption of under 500 fJ for a single programming event.

EIS transistors with a three-terminal structure facilitate non-distributed and linear weight update by employing separate terminals for programming (gate) and reading (drain). However, while these designs enhance reliability of synaptic modulation, they introduce complexities in the fabrication process and impede integration into crossbar arrays [89–91]. Baek et al. firstly developed the vertical two-terminal EIS, which enabled reliable synaptic operation comparable to the synaptic transistors based on Li-ion intercalation [92]. As depicted in Fig

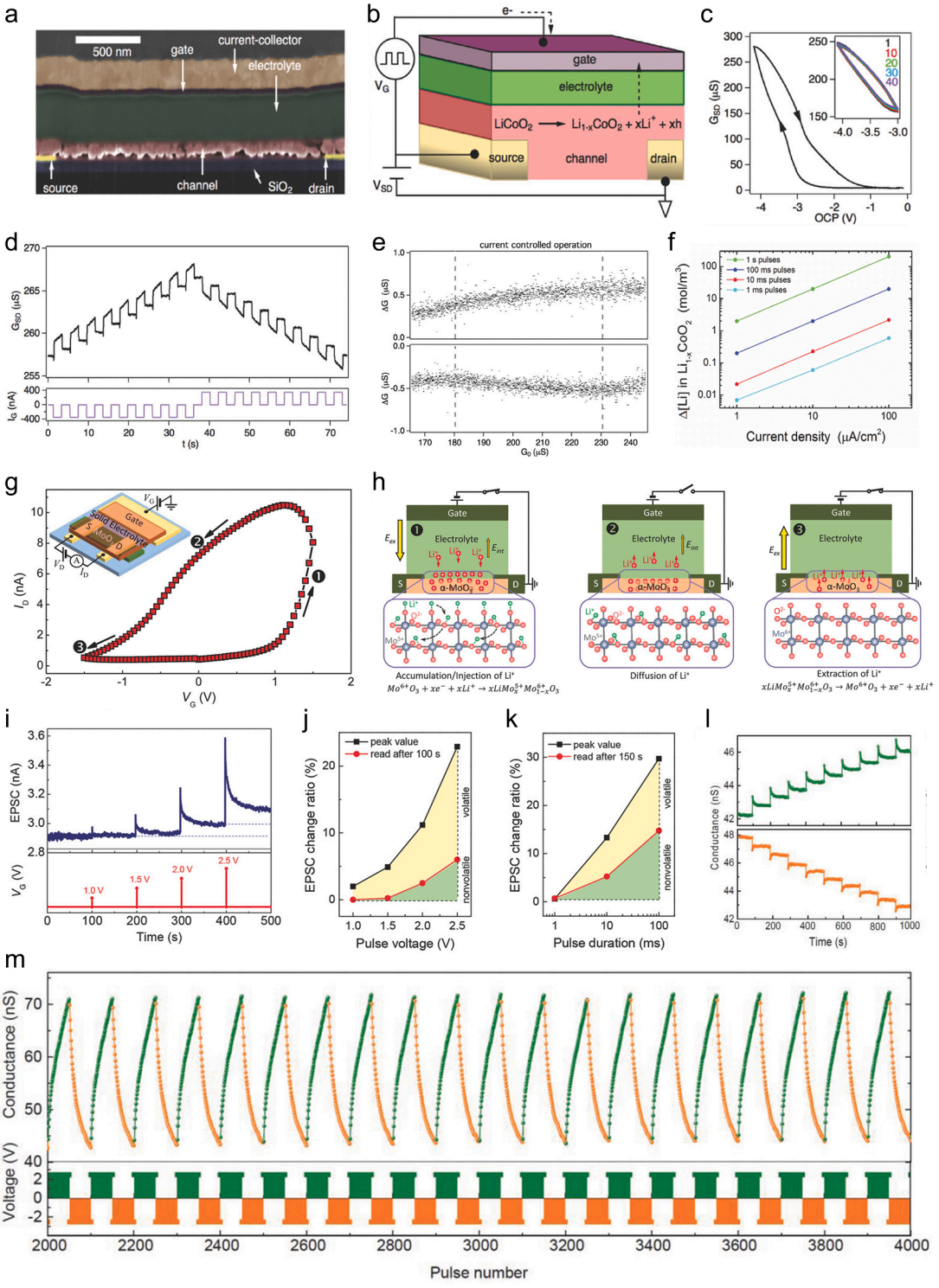

Fig. 5. Nonvolatile redox transistor based on electrochemical reaction of Li-ions. (a) Cross-sectional SEM image and (b) schematic of Li^+-based synaptic transistor. (c) Increase in source-drain conductance by a shift of open circuit potential, which is negative of V_G. The inset depicts the conductance curves over the various number of cycles (1, 10, 20, 30, and 40). (d) Source-drain conductance plot under the train of negative current pulses and subsequent positive current pulses. (e) Probability distribution plots of ΔG_M versus G_0 in potentiation (upper) and depression (lower). its uniformity. An average standard deviation is significantly low showcasing (f) The linear dependence of charge transferred on both the pulse amplitude and duration. Reproduced with permission. [41] Copyright 2016, Wiley-VCH GmbH. (g) Drain-source current dependence on the gate voltage. The inset illustrates the synaptic device with Li-ion solid electrolyte and 2D α-MoO_3 nanosheet. (h) Conductance modulation mechanism by the Li-ion injection and extraction in 2D α-MoO_3 nanosheet. (i) EPSC demonstration with same duration time and different amplitudes (1.0, 1.5, 2.0, and 2.5 V). (j) EPSC change ratio ($(I - I_0)/I_0 \times 100$ %) by varying pulse amplitudes and pulse durations, respectively. (k) Nonvolatile channel conductance showing a synaptic weight update behavior between LTP (upper) and LTD (lower). (l) Synaptic potentiation and depression of channel conductance under 50 repeated positive and negative gate voltage pulses. (m) Repeated cycles of weight updates by voltage pulses, each providing 50 synaptic potentiation and depression. Reproduced with permission. [83] Copyright 2018, Wiley-VCH GmbH.

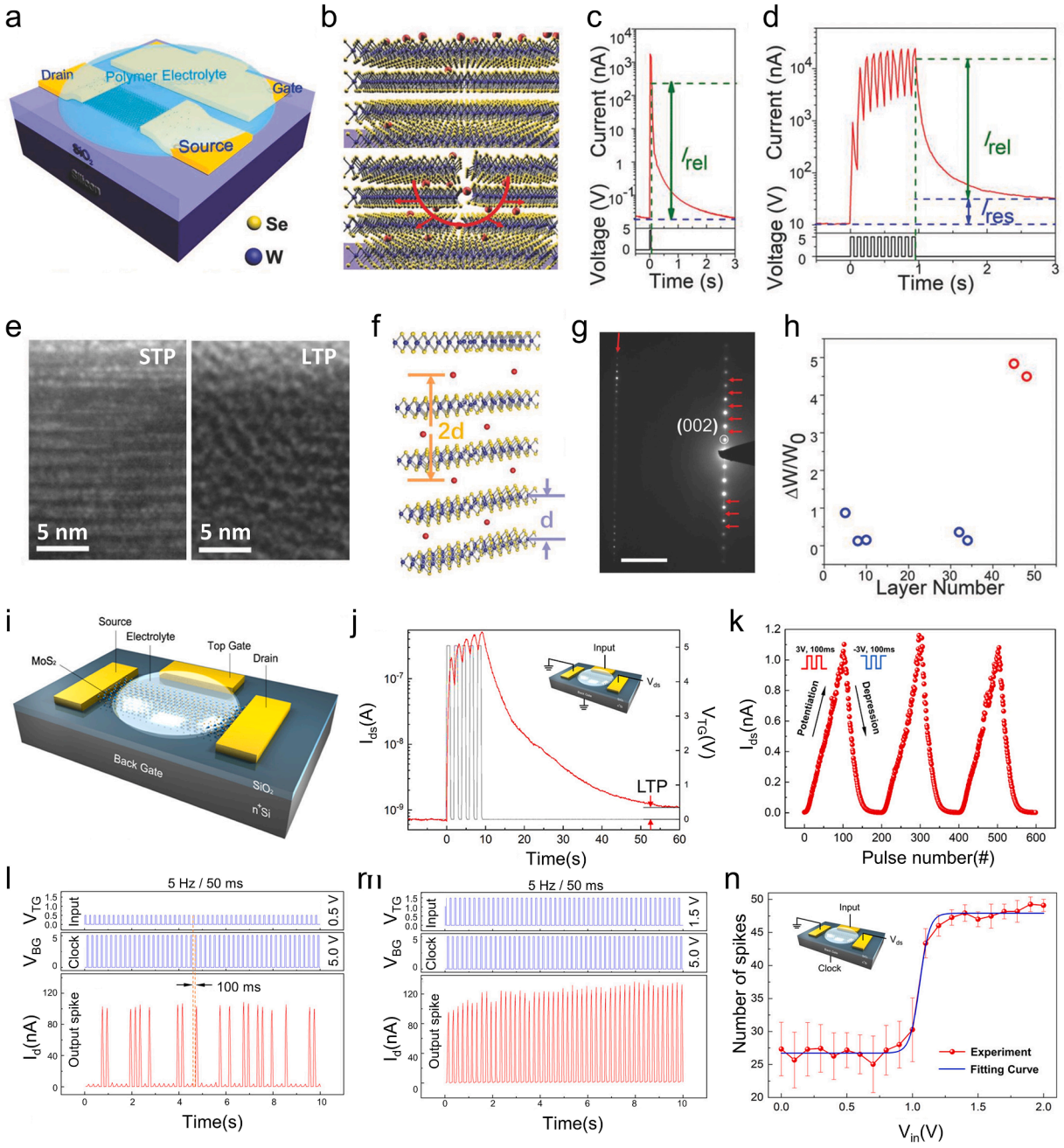

Fig. 6. Synaptic transistors based on Li-ion intercalation into 2D layered structure. (a) The configuration of an ionic-gating-modulated synaptic transistor utilizing a polymer electrolyte, where Li-ions drive in/extract from layered transitional metal dichalcogenide and phosphorus trichalcogenides, producing ionic gating effects. (b) Illustration of ionic gating mechanisms. Li-ions are diffused onto the surface of the layered crystal and absorbed temporarily resulting in short-term plasticity (upper). Li-ions are intercalated into the layered crystal, leading to long-term plasticity (lower). (c) Short-term plasticity to a single gate pulse. The drain-source current increases abruptly and immediately decays back to its initial state. (d) Long-term plasticity to the multiple programming by gate pulses. The cumulative potentiation leads to increased current states after the relaxation. (e) Cross-sectional HRTEM image of the intact layered WSe_2 structure exhibiting the short-term plasticity (left) and structural disorder in the layered WSe_2 leading to the long-term plasticity (right) . (f) Schematic depiction of Li-ion intercalation into WSe_2, attributed to a semiconducting to metallic transition. Alongside the pre-existing d-spaced WSe2 layers, an additional Li layer with a 2d spacing is observed. (g) SAED pattern of after LTP modulation of WSe_2 film displaying additional minor diffraction spots resulting from Li-ion intercalation as shown in Fig. 5f. (h) Long-term weight change dependent on the number of WSe_2 layers. Reproduced with permission. [86] Copyright 2018, Wiley-VCH GmbH. (i) Schematic illustration of the synaptic transistor based on Li^+-intercalated MoS_2. (j) Long-term plasticity in the MoS_2 synaptic transistor after applying several gate pulses. (k) Change in channel conductance during 100 potentiation and 100 depression gate pulses. Integrate-and-fire function of the MoS_2 synaptic transistor with (l) 5 V input pulse train and (m) 1.5 V input pulse train. (n) The number of output spikes in 10 s as a function of the input pulse amplitudes. Reproduced with permission. [87] Copyright 2019, American Chemical Society.

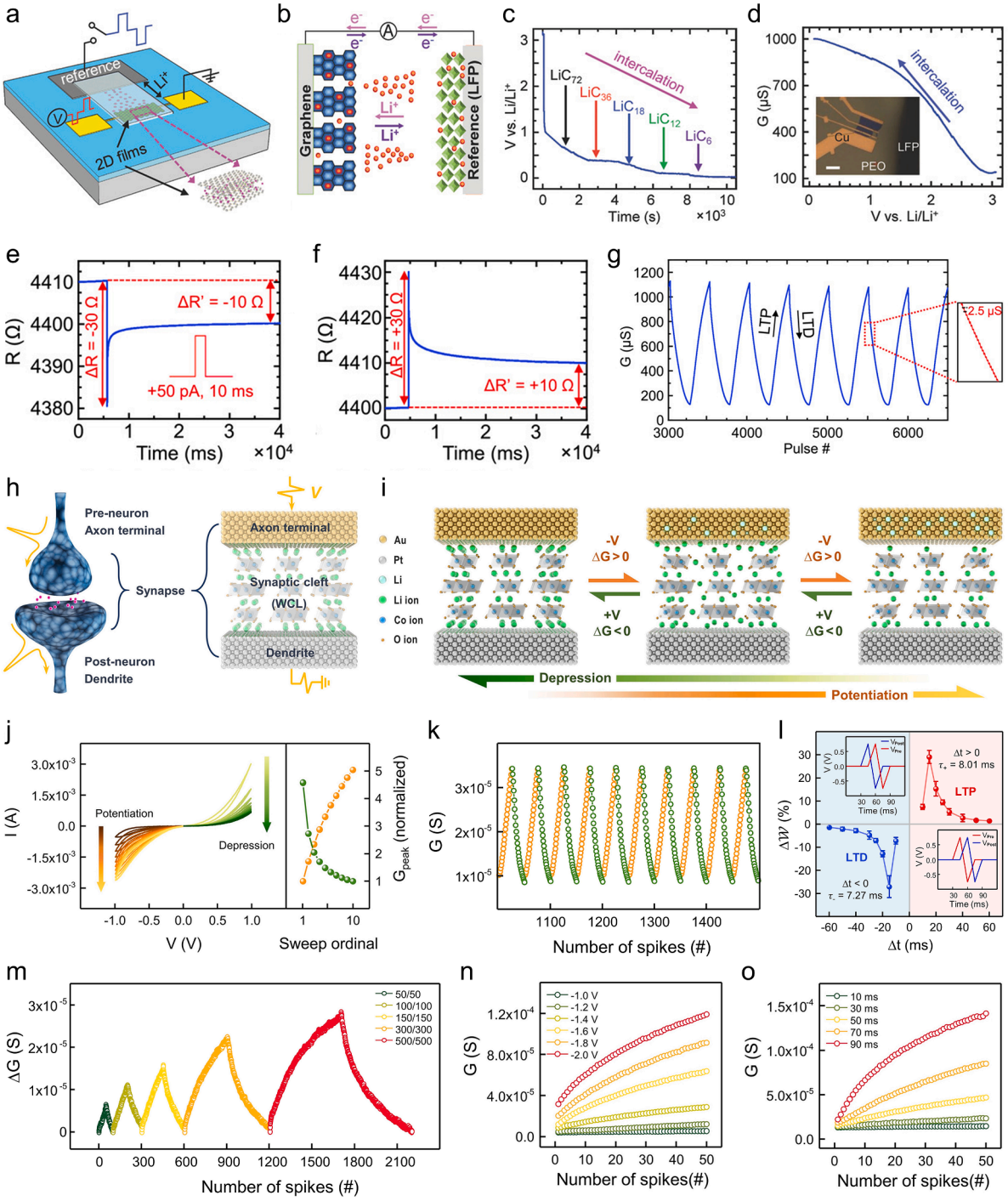

Fig. 7. Electrochemical artificial synapses based on Li-ion intercalation. (a) Schematic of electrochemical graphene synapse, where Li-ions are intercalated into few-layer graphene. (b) Illustration of the reversible electrochemical intercalation of Li-ions. (c) Galvanostatic discharge measurement of a graphite thin film in the Li-ion intercalation process. (d) Graphene conductance modulated by the electrochemical potential. The inset shows an electrochemical graphene synapse. (e) Potentiation and (f) depression characteristics in an electrochemical graphene synapse. (g) Long-term potentiation and depression behaviors through Li-ion intercalation. Reproduced with permission. [88] Copyright 2018, Wiley-VCH GmbH. (h) Schematic of two-terminal artificial synapses mimicking biological synapses. (i) Graphical illustration of the weight modulation in the Li_xCoO_2 vertical synapses. (j) Potentiation and depression behaviors during 10 negative DC sweeps and subsequent 10 positive DC sweeps. (k) Synaptic potentiation and depression through multiple pulse cycles, which consist of 25 negative spikes and the subsequent 25 positive pulses. (l) Hebbian form of spike-timing-dependent plasticity. The interval of tens of milliseconds between pre-leading-post and post-leading-pre spikes leads to long-term potentiation and depression, respectively. (m) Spike-number-dependent plasticity determined by the number of weight control spikes. (n) Spike-voltage-dependent plasticity determined by the amplitudes of weight control spikes. (o) Spike-width-dependent plasticity determined by the duration of weight control spikes. Reproduced with permission. [92] Copyright 2023, Springer Nature.

7h, the simple vertical Au/$LiCoO_2$/Pt structure closely resembles the biological synapse, featuring a gap between the presynaptic neuron and the postsynaptic neuron. Synaptic potentiation and depression were demonstrated by controlling the dearth of Li-ion in Li_xCoO_2 weight control layer in progression. Fig. 7i illustrates the weight control mechanism in Au/$LiCoO_2$/Pt EISs. Applying a negative voltage causes Li cations to deintercalate from Li_xCoO_2 and be inserted into the Au top electrode, increasing conductance. Conversely, when a positive voltage is applied, the Au-inserted Li cations are extracted and re-intercalated into the Li_xCoO_2 layer, leading to the restoration of the increased conductance to its initial state. At this time, the Li_xCoO_2 thin film was deposited in a (003) orientation that was favorable for ion diffusion within the grain with a fine grain size of ~20 nm in order to minimize the ion migration path and maximize nonvolatile properties. As shown in Fig. 7j, a 5-fold gradual increase and decrease in device conductance were achieved over 20 successive DC voltage sweeps. Likewise, spike voltage-induced LTP/LTD weight updates were emulated in a linear and symmetric manner as displayed in Fig. 7k. Various synaptic plasticities depending on the activity pattern of weight control spikes were further explored. In particular, the vertical two-terminal structure facilitates the demonstration of STDP characteristics, a weight specialization based on a firing order of presynaptic and postsynaptic neurons. As shown in Fig. 7l, STDP properties were realized by simultaneously applying staggered active spikes to the top electrode, serving as the presynaptic neuron, and the bottom electrode, representing the postsynaptic neuron. Furthermore, the SNDP, SVDP, and SWDP properties can be investigated by adjusting the quantity, amplitude, and duration of weight control spikes, as depicted in Fig. 7m to o. The consistent and stable synaptic modulation, which highly depends on the activity pattern, underscores the excellent weight controllability of the vertical two-terminal EIS device.

5. Na^+-based EISs

Although Na intercalation system has been explored considerably less than Li intercalation system, Na is an attractive option for various applications when a large amount of alkali is required for large-scale applications due to its naturally abundance and cost-effectiveness [93–95]. Consequently, there have been numerous endeavors to harness the potential of solid-state systems employing reasonably priced Na-ion technology [96–99]. Moreover, in biological synapses, Na^+ influx is responsible for the generation of action potential in the pre-synaptic membrane, which leads to neurotransmission at the synaptic terminal. Utilizing Na-based synaptic devices is crucial for faithfully replicating the diverse plasticity mechanisms observed in biological synapses.

Wang et al. demonstrated EIS transistors based on Na-ion diffusion in solid-state electrolytes [100]. To achieve thermally and chemically stable synaptic devices, an alkali metal-based inorganic electrolyte, Na^+-diffused SiO_2 layer, and 2D monolayer, MoS_2 was adopted, as depicted in Fig. 8a. The Na-ions in $Na_2O{\cdot}xSiO_2$, located at the surface of the SiO_2 layer, migrate into the inside of SiO_2 upon negative V_G. The

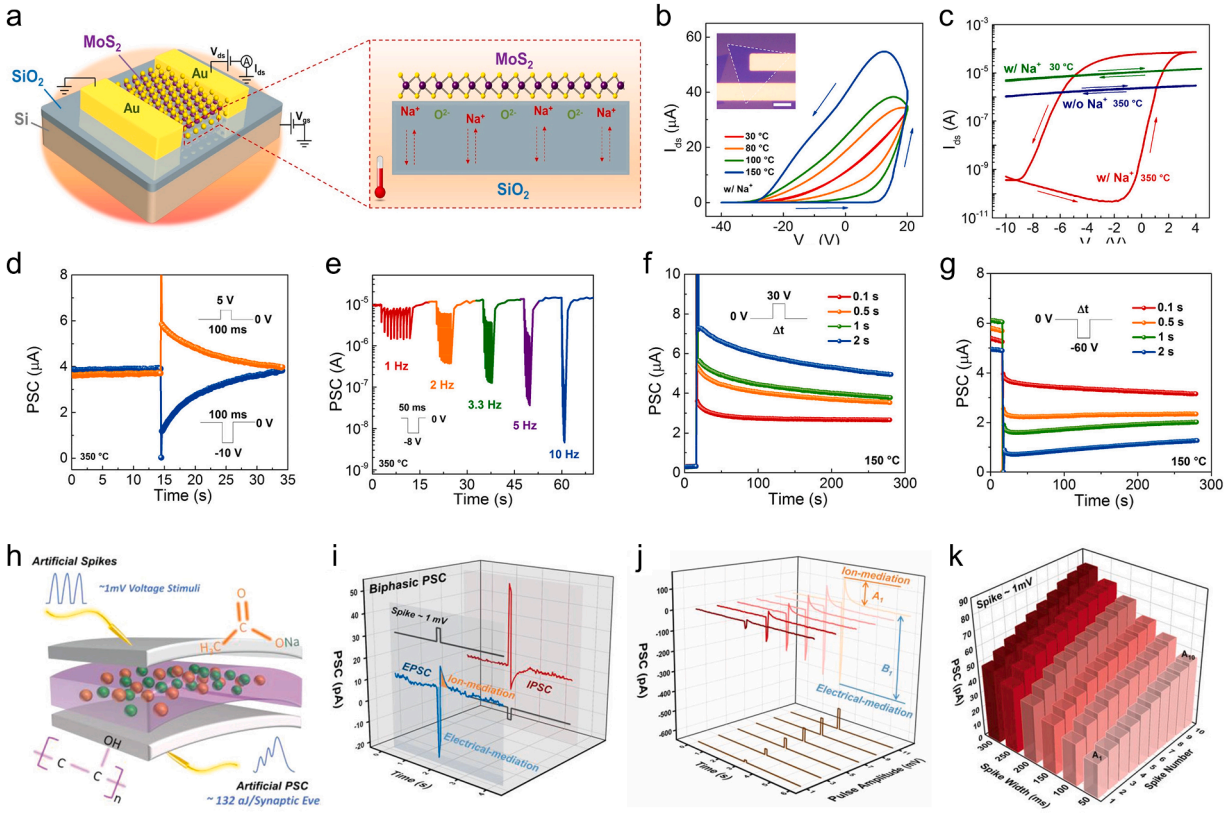

Fig. 8. Synaptic devices based on Na-ion diffusion in the channel. (a) Schematic illustration of the mechanism in the synaptic transistor based on MoS_2/Na^+-diffused SiO_2 layers. (b) Temperature-dependent transfer curves of the MoS_2/Na^+-diffused SiO_2 transistor. The inset is the optical image of the synaptic transistor. (c) I_{ds}–V_{gs} curves of the MoS_2/Na^+-diffused SiO_2 transistor. (d) Postsynaptic currents induced by +5 and −10 V pulses, relaxing back to initial states in 20 s. (e) Postsynaptic currents with varying frequencies of 10-pulse stimuli. (f) Increases in postsynaptic currents after positive pulses with different durations. (g) Decreases in postsynaptic currents after negative pulses with different durations. Reproduced with permission. [100] Copyright 2021, American Chemical Society. (h) Schematics of NaAc-doped PVA artificial synapse. Synaptic functions are attributed to Na-ions from doped NaAc salt. (i) Biphasic postsynaptic currents consisting of an initial depolarizing current followed by a hyperpolarizing component. (j) Biphasic postsynaptic currents respond to the voltage spikes with various amplitudes ranging from 1 to 11 mV. (k) Ion-mediated postsynaptic currents of 10 successive spikes with varying spike duration. Reproduced with permission. [101] Copyright 2021, Wiley-VCH GmbH.

electron density of the n-type MoS_2 channel diminishes by space change of remaining O^{2-}, leading to a low conductance state [93]. On the other hand, a high conductance state is achieved by applying positive V_G, which induces an increase in electron density with the reverse migration of Na-ions back to the SiO_2 surface. The diffusion of Na-ions within the SiO_2 film shows temperature dependence. Initially, Na-ions exhibited very limited mobility at 30 °C, as shown in Fig. 8b. They froze in the SiO_2 layer at low temperatures. However, as temperature increased, Na-ions became more active, exhibiting an anticlockwise hysteresis in the I_D-V_G curve. At higher temperatures, their migration within the SiO_2 layer became feasible upon voltage gating. In Fig. 8c, the MoS_2 EIS incorporation of Na-ions shows a huge on/off ratio of 10^6 at 350 °C, while the device without Na-ions displays almost no variation in its I_D-V_G curve. As illustrated in Fig. 8d, the post-synaptic currents (PSCs) at 350 °C were stimulated by gate pulses of +5 V and −10 V with 100 ms duration and relaxed back to their initial states in 20 s. This short-term memory behavior is attributed to the accumulation and depletion of Na-ions by the voltage stimuli, followed by their spontaneous diffusion to their original states. In Fig. 8e, the MoS_2 EIS was subjected to 10 pulses with varying frequencies to emulate the synaptic functions of a low-pass filter. As the frequency increased, the amplitudes of the PSCs decreased, indicating their suppression, whereas low-frequency stimuli were able to pass through. Furthermore, as displayed in Fig. 8f and g, the synaptic transistor shows long-term plasticity at a relatively lower temperature of 150 °C, where the mobility of Na-ions is significantly reduced. Since larger values of positive and negative V_G should be required at 150 °C than that of 350 °C, specifically 30 V and −60 V pulses were used for LTP and LTD, respectively. In Fig. 8f, low-level PSC states were modulated to a higher state by the positive V_G, and this changed state remained stable over time without decaying to the initial state, demonstrating retention characteristics. In Fig. 8g, LTD was achieved using a negative gate pulse. The PSCs observed in both Fig. 8f and g are dependent on the pulse duration, with longer pulse durations resulting in more significant increments in LTP and LTD. This is due to the increased migration of Na-ions into the SiO_2 matrix or the SiO_2 surface during LTP or LTD, respectively, when pulse duration is extended.

In pursuit of achieving ultra-low energy consumption at the attojoule scale, Hu and colleagues presented a two-terminal EIS using a simple metal-insulator-metal (MIM) sandwich structure [101]. Fig. 8h illustrates the schematic structure of the device, featuring Mo electrodes and a layer of polyvinyl alcohol (PVA) doped with sodium acetate (NaAc) salt, situated between two layers of Mo electrodes. With resemblance to biological synapses, the addition of NaAc to the PVA allows mobile Na-ions to mimic the process of neurotransmitter release at the presynaptic membrane. It's noteworthy that while various artificial synapses have primarily demonstrated monophasic PSCs, this NaAc-doped PVA synapse achieves biphasic PSCs [102–105]. In the biological context, the potential across the cell membrane is consistently maintained with negative inside and positive outside, resulting in a constant relative polarity. Depolarization occurs when the inside potential becomes more positive, leading to EPSC, while hyperpolarization, generated by a more negative inside potential, induces inhibitory postsynaptic currents (IPSC) [106–108]. This two-terminal EIS emulates these fundamental biological processes effectively. Fig. 8i exhibits the behavior of the NaAc-doped PVA synapse, displaying biphasic PSC akin to EPSC and IPSC in biological synapses. An initial depolarization (1 mV spike) succeeded by a subsequent hyperpolarization (−1 mV spike) generates EPSC, while the inverse sequence, an initial hyperpolarization followed by depolarization, results in IPSC. In biological synapses, biphasic currents consist of an electrically mediated component and a subsequent neurotransmitter-mediated component [109,110]. In the NaAc-doped PVA electrolyte, this behavior is replicated through the manipulation of electrical fields and ion transport, effectively simulating both electrical and neurotransmitter mediation. Fig. 8j represents the amplitude-dependent modulation of biphasic current. The alteration of both the ion-mediated and electrically-mediated components of the PSC was adjusted by controlling the amplitude of the spike. SWDP was demonstrated by the NaAc-doped PVA synaptic device. In Fig. 8k, a series of 10 consecutive pulses increasing spike width, with a constant frequency and amplitude, were delivered to the device, and the ion-mediated components of PSC were measured. The amplitude of PSC exhibits an increase as the spike width becomes longer. However, the rise of synaptic weights, which is normalized to the initial PSC (A_{10}/A_1), was reduced as the spike width increased. A reduction in PSC gain as spike length increases indicates that synaptic weight enhancement is diminished in response to extended periods of individual stimulation. Biological neurons tend to exhibit a more intense response to novel stimuli compared to prolonged, unchanging activity [93]. It shows a resemblance to the biological phenomenon where the synapses are significantly affected by short-duration activity with high frequency.

As observed in previous EIS transistors, the infiltration of Na-ions into the WO_x channel region leads to synaptic weight updates. Hwang's group demonstrated the feasibility of Na^+-based EIS by conducting a detailed comparison of linearity and retention performance based on whether Li-ions or Na-ions were involved [111]. Fig. 9a depicts the schematic of an all-solid-state Na^+-based synaptic transistor (NST), consisting of a WO_x channel, an Al_2O_3 barrier layer, a $NaWO_3$ electrolyte layer, and a W gate electrode. The Na-ions from the electrolyte can intercalate into and be extracted from the WO_3 channel area. Fig. 9b represents the transfer curve (I_D-V_G) of the NSTs. With a larger $+V_G$ applied, I_D increases due to the doping of Na-ions into the channel area. A further growth in V_G induces a higher I_D with more movement of cation to the WO_x channel. The repetitive LTP/LTD modulation in NST and Li^+-based synaptic transistor (LST) is shown in Fig. 9c. The NST displays better linearity than the LST due to the more precise control of heavier Na-ions than lighter Li-ions. The retention characteristics of NST and LST are confirmed in Fig. 9d, where it is evident that the retention of NST is less degraded than that of LST. The lower ionic diffusivity of Na-ions in WO_3 compared to Li-ions contributes to the improved retention property.

Metal chalcogenide SnS_2, with its 2D layered structure and large interlayer spacing, provides a conducive environment for cation insertion and extraction [112]. Jang et al. have developed an EIS transistor that utilizes layered SnS_2-reduced graphene oxide (RGO) composites, enabling the reversible uptake and release of Na-ions [113]. Fig. 9e illustrates a three-terminal EIS comprised of a layered SnS_2-RGO channel, Na^+-doped polyethylene oxide (PEO) electrolyte, and an Al gate electrode. As shown in Fig. 9f, increasing a positive gate pulse, Na^+, and ClO_4^- ions in PEO electrolyte move in different directions according to their polarities. As a result, an EDL in the electrolyte layer is formed, consisting of an electric-neutral region and an ionic-polar region. Further increase in gate potential leads to intercalation of the accumulated Na-ions into the SnS_2-RGO channel. The conductance state of the channel is modified by the electrochemical reaction of Na-ions in the SnS_2-RGO layer. The schematic of the mechanism is illustrated in Fig. 9g. When gate potential decreases, the reverse electrochemical reaction of Na-ions occurs, leading to their extraction from the channel area. In Fig. 9h, the SnS_2-based EIS transistor shows uniform synaptic weight modulation behavior for 36 cycles of potentiation and depression pulses. The weight update in synapses is decided by the summation of the spatiotemporal inputs, as presented in Fig. 9i. Therefore, to accomplish the spatiotemporal learning, multi-gate inputs were utilized in the SnS_2-based synaptic transistor. With three types of spatiotemporal patterns of pulses ($\Delta t < 0$, $\Delta t = 0$, or $\Delta t > 0$) shown in Fig. 9j, the PPF index was calculated by the update ratio of EPSCs as a function of Δt. Fig. 9k presents that the EPSC amplitude peaked at its maximum value when $\Delta t = 0$, resulting in the highest PPF index. On the other hand, an increase in $|\Delta t|$ yields a gradual decrease in amplitudes of EPSC and PPF index. Hence, it fully emulates the biological synaptic functions interpreting and processing temporal data.

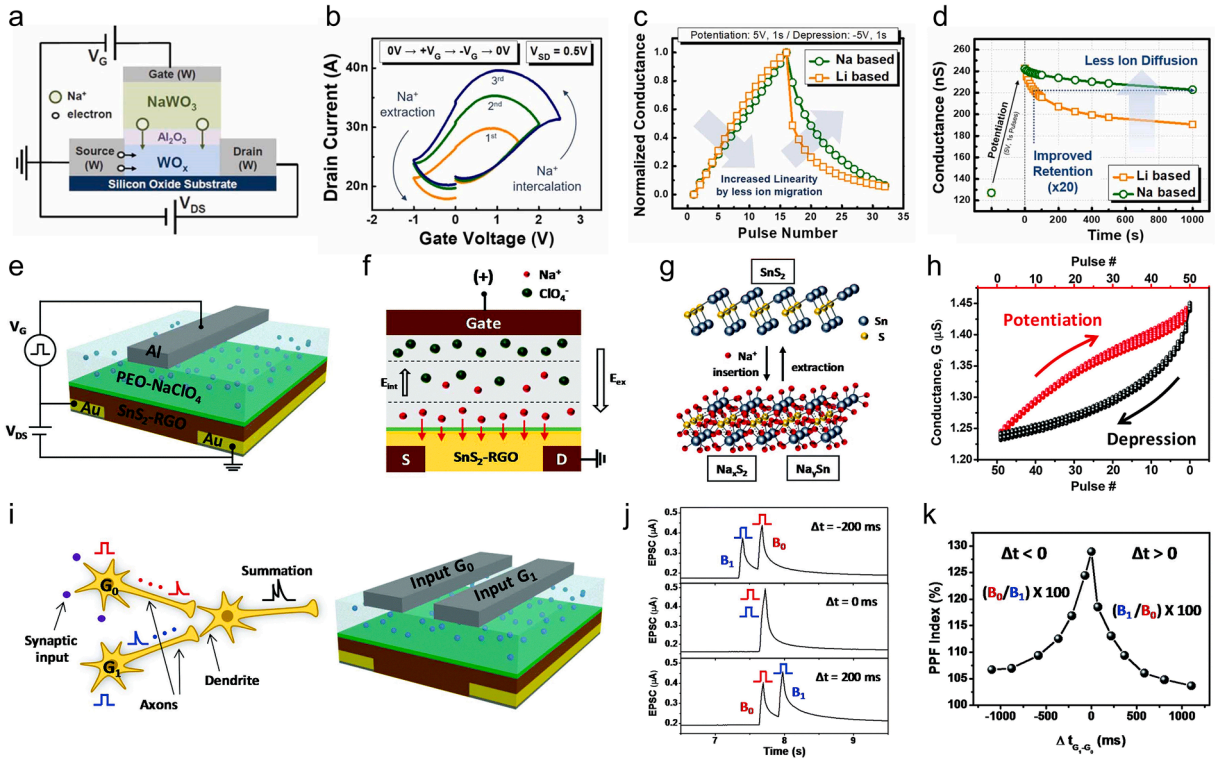

Fig. 9. Artificial synapses with electrochemical insertion of Na-ions. (a) Schematics of all-solid-state Na^+-based synaptic transistor. (b) Transfer curve (I_D–V_G) of Na^+-based synaptic transistor. An increase in V_G leads to more intercalation of Na-ions. (c) Synaptic weight update behavior of Na^+ ion-based and Li^+-based synaptic transistors. Na^+ -based synapses exhibit better linearity. (d) Retention measurement of Na^+-based and Li^+-based synaptic transistors. Conductance is less degraded in Na^+-based synapses. Reproduced with permission. [111] Copyright 2020, IOP Publishing. (e) Schematic illustration of artificial synapses with SnS_2-RGO and Na^+-doped polyethylene oxide (PEO) electrolyte. (f) Conductance change mechanism through the migration of Na-ions and their intercalation into the channel. (g) An insertion and extraction of Na-ions within SnS_2. (h) Potentiation and depression of channel conductance by the 50 sequential positive and negative pulses. (i) Schematics of spatiotemporal neural networks and artificial synaptic transistors with two presynaptic input gates. (j) Excitatory postsynaptic current by three types of pulse pattern with two spatiotemporally presynaptic inputs. (k) PPF index plotted by the amplitude of excitatory postsynaptic current with varying the pulse interval. Reproduced with permission. [113] Copyright 2019, Royal Society of Chemistry.

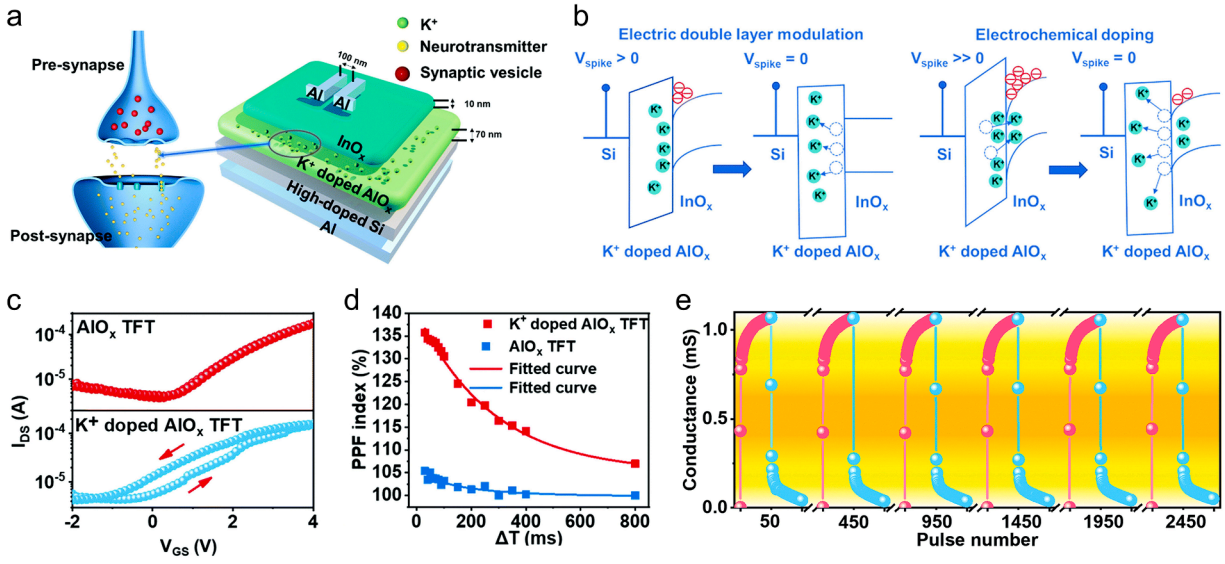

Fig. 10. Conductance change via migration of K-ions into the channel. (a) Schematic illustration of the electrochemical artificial synaptic TFTs based on K^+-doped AlO_x dielectric and InO_x semiconductor. (b) The mechanism of channel conduction change by spike-induced K-ions migration in the K^+-doped AlO_x. (c) Transfer characteristic curves and (d) PPF index as a function of the spike interval of the TFTs with or without K^+-doped AlO_x dielectric layer. (e) Stability test during 25-pulse cycles, one of which consists of 50 positive and subsequent 50 negative pulses, showcasing that synaptic behavior remains after 2500 pulses. Reproduced with permission. [116] Copyright 2022, Royal Society of Chemistry.

6. K^+-based EISs

In biological synapses, K-ions have a critical role in setting the resting membrane potential, and oppose depolarization from rest [114,115]. Their movement through potassium channels is tightly regulated and is fundamental for proper neuronal signaling.

Cao et al. showcased solution-based thin-film transistors EIS that operate on K-ion conduction within the AlO_x dielectric layer, exhibiting iontronic behavior similar to biological synapses [116]. Fig. 10a depicts the EIS thin-film transistors based on InO_x n-type channel semiconductor and K-ion doped AlO_x dielectric. Both InO_x and AlO_x thin films were fabricated using a solution-based method. Similar to biological synapses, the mobile K-ions serve as neurotransmitters, altering channel conductance. The weight control mechanism, analogous to aforementioned EIS TFTs, is proposed in Fig. 10b. The K-ions within the AlO_x dielectric diffuse toward the AlO_x/InO_x interface when a positive voltage spike (V_{spike}) is applied to the gate. These relocated K-ions change the channel conductance through two distinct processes of ionic electronic modulation, depending on the intensity of the V_{spike}: EDL modulation as STP and electrochemical doping as LTP. When a V_{spike} is applied, the K-ions being transported temporarily aggregate at the AlO_x/InO_x interface. This ion accumulation results in an increased concentration of channel electrons, therefore, an enhancement of channel conductance. When the external electric field was removed, the concentration gradient let the gathered K-ions quickly diffuse back to their original state, causing the EDL to disappear. Conversely, with a strong V_{spike}, some of the K-ions infiltrate into the InO_x channel, raising channel conductance. Consequently, these infiltrated K-ions persist inside the channel even after the V_G is withdrawn, maintaining enhanced channel conductance for an extended duration. Fig. 10c displays the transfer curves of the EIS TFTs, both with and without the K-ions doped AlO_x dielectric. Due to the influence of K-ion migration, devices with K-ion doping show a more pronounced hysteresis window in the counterclockwise direction compared to devices without K-ion doping. The PPF characteristics presented in Fig. 10d further confirm the effectiveness of mobile K-ions by showing that K-ion-doped AlO_x TFT exhibits superior synaptic sensitivity. Despite the advantageous iontronic biosimilarity, the K-ion-based EIS exhibited non-linear and asymmetric non-linear and asymmetric LTP/LTD weight updates, as presented in Fig. 10e. This implies a need for further improvement to enhance the performance of neuromorphic computing.

7. Summary and perspectives

An urgent demand for hardware neuromorphic systems has prompted the exploration of various platforms for the implementation of artificial synapses. With iontronic resemblance to the electrochemical mechanisms in biological synapses, EISs have emerged as promising candidates due to the fine controllability of synaptic weights. Mobile ions in EISs, which are inserted into and extracted from active areas, can be precisely modulated more dynamically and reversibly. Therefore, EISs for programmable analog hardware are a potential candidate for low-powering and high-accuracy neural network accelerators. A wide range of active species, including protons and alkali ions, were employed to mimic a variety of synaptic functions within three-terminal and two-terminal EIS devices. Table 1 provides a comprehensive comparison of the performance indicators for EIS devices as examined in the manuscript. Unlike preceding studies based on ReRAM, PCM, and ferroelectric, EISs can harvest versatile benefits with tiny and gradual modifications in conductance states suitable for massive analog computing. Although unique properties, significant progress is still required before their field can attain full maturity. Hence, we suggest the perspectives across multiple dimensions guide the advancement of EISs.

7.1. Materials and device engineering

The majority of EISs demonstrate enhanced linearity and controllability compared to their predecessors, primarily attributable to their gradual conductance modulation. EISs utilizing H^+ and Li^+ ions offer the advantages of low power consumption and rapid operational speeds, attributed to the lighter mass of the active ions. Moreover, the diminutive size of these ions contributes to superior storage capacities. Consequently, the manifestation of numerous multi-states, alongside distinguished features such as low power requirements and high-speed operation, makes H^+ and Li^+-based EIS systems favorable candidates for analog memory applications within neuromorphic hardware. Conversely, EIS devices that incorporate larger and heavier ions, such as Na^+ and K^+, tend to exhibit higher energy demands and reduced operation speeds. Nonetheless, the larger ionic sizes may facilitate enhanced linearity in ion transport, since they are less susceptible to voltage fluctuations. Furthermore, suppressed spontaneous ion diffusion enhances the retention capabilities of these systems. As a result, Na^+ and K^+-based EIS devices exhibit traits that are optimally suited for applications in non-volatile ssmemory technologies, despite their inherent challenges.

CMOS compatibility is another major issue in EISs, which contain vulnerable materials to polar solvents and extreme temperatures. While EISs have demonstrated their compatibility with micro-lithography processes for electrodes, the patterning of electrolytes and ionic reservoirs remains problematic due to material vulnerabilities. Therefore, there is an imminent need to develop novel materials that offer both robust device performance and fabrication stability. Recent EISs incorporating 2D channels and barriers, such as hBN and WSe_2 [74,86], show promising solutions due to their rapid adaptive behavior and enhanced

Table 1
Comparative analysis of the performance metrics of EIS devices discussed in the manuscript.

Active ion	Materials		Active size	Operating pulse	Dynamic range	Energy cost	Ref.
H^+	Nafion	WO_3	500 μm × 100 μm	±0.5 μA / 5 ms	5 ~ 42 μS	0.39 fJ/μm^2	[66]
	Phosphosilicate glass	WO_3	5 μm × 50μm	±3 V / 1 s	0.7 ~ 1 μS	6.75 fJ/μm^2	[70]
	Silica	$NdNiO_3$	200 μm × 20 μm	+0.7 V, −1.0 V / 5 s	300 ~ 500 μS	0.45 fJ/μm^2	[73]
	Si-H/hBN	WO_3	20 μm × 10 μm	± 1 V / 10 ms	8.36 ~ 10.53 μS	–	[74]
	PVA-H_2SO_4	$(Ti_3C_2T_x$ Mxene/TAPA$)_n$	20 μm × 1000 μm	± 1 V / 4 μs	1.6 ~ 2.75 mS	80 fJ/μm^2	[75]
Li^+	LiPON	$LiCoO_2$	2 μm × 25 μm	±0.75 mV / 2 s	150 ~ 250 μS	20 pJ/μm^2	[41]
	PEO:$LiClO_4$	α-MoO_3	5 μm × 10 μm	±2.5 V / 10 ms	42 ~ 75 nS	36 nJ/μm^2	[83]
	PEO:$LiClO_4$	WSe2	1 μm × 3 μm	+1.2 V, −0.4 V / 100 ms	250 ~ 570 pS	10 fJ/μm^2	[86]
	PEO:$LiClO_4$	MoS2	2 μm	±3 V / 100 ms	0.1 ~ 11 nS	0.5 nJ	[87]
	PEO:$LiClO_4$	Graphene	4 μm × 15 μm	±50 pA / 10 ms	150 ~ 1150 μS	13.9 fJ/μm^2	[88]
	$LiCoO_2$		50 μm × 50 μm	+1.1 V, −1.5 V / 10 ms	8 ~ 35 μS	1.6 nJ/μm^2	[92]
Na^+	SiO_2	MoS2	–	−30 V, +10 V / 100 ms	1.8 ~ 3.8 μS	–	[100]
	PVA:NaAc		–	±1 mV / 100 ms	110 ~ 220 pS	132 aJ	[101]
	$NaWO_3/Al_2O_3$	WO_3	120 μm × 120 μm	±5 V / 1 s	90 ~ 150 μS	–	[111]
	PEO:Na^+	SnS_2-RGO	100 μm	0~2 V, 0~−0.2 V / 50 ms	1.23 ~ 1.45 μS	–	[113]
K^+	AlO_x:K^+	InO_x	10 μm × 150 μm	+4 V, −2 V / 15 ms	40 ~ 1100 μS	–	[116]

material durability. It is anticipated that the application of inorganic electrolytes with 2D layered structures will help overcome the limitations associated with material used in diverse EIS applications.

7.2. Scalability and array integration

In recent studies, the device scale in EISs remains at a few micrometers. While there is an expectation that nanoscale devices will require an ultra-low 4 aJ for their switching energy, which is even lower than that of biological synapses [88], there is currently no comprehensive study on nanoscale EISs. Additionally, the three-terminal structure has been the dominant architecture in recently reported EISs. In efforts to reduce the effective area further, two-terminal EISs have been successfully demonstrated [92]. The implementation of a crossbar array with memristor structures presents an efficient strategy for achieving high-density neuromorphic hardware.

The absence of compatibility with CMOS technology has hindered the integration of EISs into an array. To advance the maturity of this field, practical array demonstrations should be undertaken. The first notable demonstration of array integration was achieved by Li et al. [117], who created a small 3 × 3 crossbar array to enhance learning acceleration. However, the development of large-scale arrays remains in the simulation phase and has not yet been realized with physical hardware.

7.3. Manufacture and commercialization

Owing to their superior linearity, minimized variability, and information storage capacity of EISs relative to other two-terminal (ReRAM, PCM) and three-terminal devices (field-effect transistors), EISs are anticipated to become a focal point of interest in the near future. Nevertheless, the feasibility of commercializing ion-tunable electronics remains uncertain at this juncture, given that there are so many fundamental and technological obstacles yet to be surmounted. It is imperative to conduct evaluations concerning the utilization of materials compatible with foundry processes, address integration challenges, and ensure congruence with monolithic fabrication methodologies aspects in the transfer of EISs from the laboratory level to commercial neuromorphic circuits.

Economic factors and performance metrics will exert a substantial influence on the trajectory towards commercialization. Metal oxides, which are currently preferred in the semiconductor memory market due to their cost-efficiency in production, highlight the potential of EIS technologies, which are predominantly based on these materials, to achieve cost-effectiveness in manufacturing processes. However, there are the escalating cost and supply risks associated with lithium. Fortunately, those have catalyzed extensive research into alternative ion-intercalation materials, notably sodium, which is plentifully available on Earth. This shift towards materials that are more readily accessible and economically viable is expected to confer a competitive edge to EIS technologies in terms of production cost efficiency in the foreseeable future.

7.4. Concluding remarks

Due to their inherent electrochemical resemblance to biological systems, EISs have attracted increasing attention among researchers. They have exhibited comparable potential to CMOS-based, resistive switching-based, and phase change-based device types, which have conventionally been the focal point of extensive research. Moreover, EISs possess the advantage of overcoming many limitations associated with transitional devices, such as stochastic nature, variability, and nonlinearity. Their superior linearity and low-power operation make them promising for diverse applications in hardware neuromorphic platfoms. While the potential of EISs in neuromorphic computing is evident, there are still several remaining inquiries concerning the design of practical systems. This review comprehensively examines the capabilities of EISs along with their fundamental and technological challenges. The collective efforts of researchers addressing these challenges are expected to propel EIS-based technology into the next generation of neural network hardware.

CRediT authorship contribution statement

Ji Hyun Baek: Conceptualization, Writing – original draft, Writing – review & editing. **In Hyuk Im:** Conceptualization, Writing – original draft, Writing – review & editing. **Eun-Mi Hur:** Funding acquisition, Writing – review & editing. **Jungwon Park:** Funding acquisition. **Jongwoo Lim:** Conceptualization. **Sangbum Kim:** Conceptualization. **Kibum Kang:** Conceptualization. **Soo Young Kim:** Funding acquisition. **Jae Yong Song:** Funding acquisition, Supervision. **Ho Won Jang:** Funding acquisition, Supervision.

Declaration of competing interest

The authors declare that they have no known competing financial interests or personal relationships that could have appeared to influence the work reported in this paper.

Data availability

The authors do not have permission to share data.

Acknowledgements

This work was supported by a research grant from Seoul National University in 2020. This work was financially supported by the Nano·-Material Technology Development Program (2022M3H4A1A01011993) through NRF (National Research Foundation of Korea), funded by the Ministry of Science and ICT. The Research Institute of Inter-University Semiconductor Research Center and Institute of Engineering Research at Seoul National University provided research facilities for this work.

References

[1] M.A. Zidan, J.P. Strachan, W.D. Lu, The future of electronics based on memristive systems, Nat. Electron. 1 (2018) 22–29, https://doi.org/10.1038/s41928-017-0006-8.
[2] S. in Yi, J.D. Kendall, R.S. Williams, S. Kumar, Activity-difference training of deep neural networks using memristor crossbars, Nat. Electron. 6 (2023) 45–51, https://doi.org/10.1038/s41928-022-00869-w.
[3] I.H. Im, J.H. Baek, S.J. Kim, J. Kim, S.H. Park, J.Y. Kim, J.J. Yang, H.W. Jang, Halide perovskites-based diffusive memristors for artificial mechano-nociceptive system, Adv. Mater. (2023) 2307334, https://doi.org/10.1002/adma.202307334 n/a.
[4] J.R. Wolpaw, N. Birbaumer, W.J. Heetderks, D.J. McFarland, P.H. Peckham, G. Schalk, E. Donchin, L.A. Quatrano, C.J. Robinson, T.M. Vaughan, Brain-computer interface technology: a review of the first international meeting, IEEE Trans. Rehabil. Eng. 8 (2000) 164–173.
[5] L.F. Nicolas-Alonso, J. Gomez-Gil, Brain computer interfaces, a review, Sensors 12 (2012) 1211–1279.
[6] F. Ye, F. Kiani, Y. Huang, Q. Xia, Diffusive memristors with uniform and tunable relaxation time for spike generation in event-based pattern recognition, Adv. Mater. 2204778 (2022) 1–7, https://doi.org/10.1002/adma.202204778.
[7] S. Kumar, X. Wang, J.P. Strachan, Y. Yang, W.D. Lu, Dynamical memristors for higher-complexity neuromorphic computing, Nat. Rev. Mater. 7 (2022) 575–591, https://doi.org/10.1038/s41578-022-00434-z.
[8] R.A. John, Y. Demirağ, Y. Shynkarenko, Y. Berezovska, N. Ohannessian, M. Payvand, P. Zeng, M.I. Bodnarchuk, F. Krumeich, G. Kara, I. Shorubalko, M. V. Nair, G.A. Cooke, T. Lippert, G. Indiveri, M.V. Kovalenko, Reconfigurable halide perovskite nanocrystal memristors for neuromorphic computing, Nat. Commun. 13 (2022) 2074, https://doi.org/10.1038/s41467-022-29727-1.
[9] S. Ambrogio, P. Narayanan, H. Tsai, R.M. Shelby, I. Boybat, C. Di Nolfo, S. Sidler, M. Giordano, M. Bodini, N.C.P. Farinha, B. Killeen, C. Cheng, Y. Jaoudi, G. W. Burr, Equivalent-accuracy accelerated neural-network training using analogue memory, Nature 558 (2018) 60–67, https://doi.org/10.1038/s41586-018-0180-5.

[10] G.W. Burr, R.M. Shelby, A. Sebastian, S. Kim, S. Kim, S. Sidler, K. Virwani, M. Ishii, P. Narayanan, A. Fumarola, Neuromorphic computing using non-volatile memory, Adv. Phys. X. 2 (2017) 89–124.

[11] E. Li, X. Wu, Q. Chen, S. Wu, L. He, R. Yu, Y. Hu, H. Chen, T. Guo, Nanoscale channel organic ferroelectric synaptic transistor array for high recognition accuracy neuromorphic computing, Nano Energy 85 (2021) 106010.

[12] G. Indiveri, B. Linares-Barranco, R. Legenstein, G. Deligeorgis, T. Prodromakis, Integration of nanoscale memristor synapses in neuromorphic computing architectures, Nanotechnology. 24 (2013) 384010.

[13] K. Sun, J. Chen, X. Yan, The future of memristors: materials engineering and neural networks, Adv. Funct. Mater. 31 (2021) 2006773.

[14] S.G. Kim, J.S. Han, H. Kim, S.Y. Kim, H.W. Jang, Recent advances in memristive materials for artificial synapses, Adv. Mater. Technol. 3 (2018) 1800457.

[15] S.H. Tan, P. Lin, H. Yeon, S. Choi, Y. Park, J. Kim, Perspective: uniform switching of artificial synapses for large-scale neuromorphic arrays, APL. Mater. 6 (2018).

[16] D.G. Roe, S. Kim, Y.Y. Choi, H. Woo, M.S. Kang, Y.J. Song, J. Ahn, Y. Lee, J. H. Cho, Biologically plausible artificial synaptic array: replicating Ebbinghaus' memory curve with selective attention, Adv. Mater. 33 (2021) 2007782.

[17] S. Ullman, Using neuroscience to develop artificial intelligence, Science 363 (2019) 692–693 (80-.).

[18] W. Zhang, B. Gao, J. Tang, P. Yao, S. Yu, M.F. Chang, H.J. Yoo, H. Qian, H. Wu, Neuro-inspired computing chips, Nat. Electron. 3 (2020) 371–382.

[19] B. Qu, A. Younis, D. Chu, Recent progress in tungsten oxides based memristors and their neuromorphological applications, Electron. Mater. Lett. 12 (2016) 715–731, https://doi.org/10.1007/s13391-016-6129-7.

[20] S.M. Hong, H.D. Kim, H.M. An, T.G. Kim, Resistive switching phenomena of tungsten nitride thin films with excellent CMOS compatibility, Mater. Res. Bull. 48 (2013) 5080–5083, https://doi.org/10.1016/j.materresbull.2013.05.073.

[21] J. Aziz, H. Kim, S. Rehman, J.H. Hur, Y.H. Song, M.F. Khan, D. kee Kim, Effect of oxygen stoichiometry on the threshold switching of RF-sputtered NbOx (x = 2.0–2.5) films, Mater. Res. Bull. 144 (2021) 111492, https://doi.org/10.1016/j.materresbull.2021.111492.

[22] Z. Wang, S. Joshi, S. Savel'Ev, W. Song, R. Midya, Y. Li, M. Rao, P. Yan, S. Asapu, Y. Zhuo, H. Jiang, P. Lin, C. Li, J.H. Yoon, N.K. Upadhyay, J. Zhang, M. Hu, J. P. Strachan, M. Barnell, Q. Wu, H. Wu, R.S. Williams, Q. Xia, J.J. Yang, Fully memristive neural networks for pattern classification with unsupervised learning, Nat. Electron. 1 (2018) 137–145, https://doi.org/10.1038/s41928-018-0023-2.

[23] K.J. Kwak, J.H. Baek, D.E. Lee, I. hyuk Im, J. Kim, S.J. Kim, Y.J. Lee, J.Y. Kim, H. W. Jang, Ambient Stable All Inorganic CsCu2I3Artificial Synapses for Neurocomputing, Nano Lett. 22 (2022) 6010–6017, https://doi.org/10.1021/acs.nanolett.2c01272.

[24] S.J. Kim, S.B. Kim, H.W. Jang, Competing memristors for brain-inspired computing, iScience 24 (2021) 101889, https://doi.org/10.1016/j.isci.2020.101889.

[25] S. Park, A. Sheri, J. Kim, J. Noh, J. Jang, M. Jeon, B. Lee, B.R. Lee, B.H. Lee, H. J. Hwang, Neuromorphic speech systems using advanced ReRAM-based synapse, in: 2013 IEEE Int. Electron Devices Meet., IEEE, 2013, pp. 25–26.

[26] I.H. Im, S.J. Kim, H.W. Jang, Memristive Devices for New Computing Paradigms, Adv. Intell. Syst. 2 (2020) 2000105, https://doi.org/10.1002/aisy.202000105.

[27] C.C. Chang, J.C. Liu, Y.L. Shen, T. Chou, P.C. Chen, I.T. Wang, C.C. Su, M.H. Wu, B. Hudec, C.C. Chang, Challenges and opportunities toward online training acceleration using RRAM-based hardware neural network, in: 2017 IEEE Int. Electron Devices Meet, IEEE, 2017, pp. 11–16.

[28] A.M.S. Tosson, S. Yu, M.H. Anis, L. Wei, Analysis of RRAM reliability soft-errors on the performance of RRAM-based neuromorphic systems, in: 2017 IEEE Comput. Soc. Annu. Symp, VLSI, IEEE, 2017, pp. 62–67.

[29] S.G. Sarwat, B. Kersting, T. Moraitis, V.P. Jonnalagadda, A. Sebastian, Phase-change memtransistive synapses for mixed-plasticity neural computations, Nat. Nanotechnol. 17 (2022) 507–513, https://doi.org/10.1038/s41565-022-01095-3.

[30] S. Ambrogio, N. Ciocchini, M. Laudato, V. Milo, A. Pirovano, P. Fantini, D. Ielmini, Unsupervised learning by spike timing dependent plasticity in phase change memory (PCM) synapses, Front. Neurosci. 10 (2016) 56.

[31] M. Suri, O. Bichler, D. Querlioz, O. Cueto, L. Perniola, V. Sousa, D. Vuillaume, C. Gamrat, B. DeSalvo, Phase change memory as synapse for ultra-dense neuromorphic systems: application to complex visual pattern extraction, in: 2011 Int. Electron Devices Meet, IEEE, 2011, p. 4.

[32] G. Li, D. Xie, H. Zhong, Z. Zhang, X. Fu, Q. Zhou, Q. Li, H. Ni, J. Wang, E. Guo, M. He, C. Wang, G. Yang, K. Jin, C. Ge, Photo-induced non-volatile VO2 phase transition for neuromorphic ultraviolet sensors, Nat. Commun. 13 (2022) 1729, https://doi.org/10.1038/s41467-022-29456-5.

[33] Z. Wang, H. Wu, G.W. Burr, C.S. Hwang, K.L. Wang, Q. Xia, J.J. Yang, Resistive switching materials for information processing, Nat. Rev. Mater. 5 (2020) 173–195, https://doi.org/10.1038/s41578-019-0159-3.

[34] S. Song, A. Das, Design methodologies for reliable and energy-efficient PCM systems, in: 2020 11th Int. Green Sustain. Comput. Work, IEEE, 2020, pp. 1–3.

[35] R.M. Shelby, G.W. Burr, I. Boybat, C. Di Nolfo, Non-volatile memory as hardware synapse in neuromorphic computing: a first look at reliability issues, in: 2015 IEEE Int. Reliab. Phys. Symp., IEEE, 2015, pp. 6A–61.

[36] Z. Luo, Z. Wang, Z. Guan, C. Ma, L. Zhao, C. Liu, H. Sun, H. Wang, Y. Lin, X. Jin, Y. Yin, X. Li, High-precision and linear weight updates by subnanosecond pulses in ferroelectric tunnel junction for neuro-inspired computing, Nat. Commun. 13 (2022) 1–11, https://doi.org/10.1038/s41467-022-28303-x.

[37] S. Boyn, J. Grollier, G. Lecerf, B. Xu, N. Locatelli, S. Fusil, S. Girod, C. Carrétéro, K. Garcia, S. Xavier, J. Tomas, L. Bellaiche, M. Bibes, A. Barthélémy, S. Saïghi, V. Garcia, Learning through ferroelectric domain dynamics in solid-state synapses, Nat. Commun. 8 (2017) 14736, https://doi.org/10.1038/ncomms14736.

[38] S. Oh, T. Kim, M. Kwak, J. Song, J. Woo, S. Jeon, I.K. Yoo, H. Hwang, $HfZrO_x$-based ferroelectric synapse device with 32 levels of conductance states for neuromorphic applications, IEEe Electron. Device Lett. 38 (2017) 732–735, https://doi.org/10.1109/LED.2017.2698083.

[39] B. Tian, L. Liu, M. Yan, J. Wang, Q. Zhao, N. Zhong, P. Xiang, L. Sun, H. Peng, H. Shen, A robust artificial synapse based on organic ferroelectric polymer, Adv. Electron. Mater. 5 (2019) 1800600.

[40] E.J. Fuller, S.T. Keene, A. Melianas, Z. Wang, S. Agarwal, Y. Li, Y. Tuchman, C. D. James, M.J. Marinella, J.J. Yang, A. Salleo, A.A. Talin, Parallel programming of an ionic floating-gate memory array for scalable neuromorphic computing, Science 364 (2019) 570–574, https://doi.org/10.1126/science.aaw5581 (80-.).

[41] E.J. Fuller, F. El Gabaly, F. Léonard, S. Agarwal, S.J. Plimpton, R.B. Jacobs-Gedrim, C.D. James, M.J. Marinella, A.A. Talin, Li-ion synaptic transistor for low power analog computing, Adv. Mater. 29 (2017) 1–8, https://doi.org/10.1002/adma.201604310.

[42] D.A. Robinson, M.E. Foster, C.H. Bennett, A. Bhandarkar, E.R. Webster, A. Celebi, N. Celebi, E.J. Fuller, V. Stavila, C.D. Spataru, D.S. Ashby, M.J. Marinella, R. Krishnakumar, M.D. Allendorf, A.A. Talin, Tunable intervalence charge transfer in ruthenium prussian blue analog enables stable and efficient biocompatible artificial synapses, Adv. Mater. 2207595 (2022) 1–13, https://doi.org/10.1002/adma.202207595.

[43] M. Shin, Y. Wang, J.R. Borgus, B.J. Venton, Electrochemistry at the Synapse, Annu. Rev. Anal. Chem. 12 (2019) 297–321.

[44] M.P. Mattson, Neurotransmitters in the regulation of neuronal cytoarchitecture, Brain Res. Rev. 13 (1988) 179–212.

[45] S. Seo, J.J. Lee, H.J. Lee, H.W. Lee, S. Oh, J.J. Lee, K. Heo, J.H. Park, Recent progress in artificial synapses based on two-dimensional van der Waals materials for brain-inspired computing, ACS Appl. Electron. Mater. 2 (2020) 371–388, https://doi.org/10.1021/acsaelm.9b00694.

[46] J. Yu, X. Yang, G. Gao, Y. Xiong, Y. Wang, J. Han, Y. Chen, H. Zhang, Q. Sun, Z. L. Wang, Bioinspired mechano-photonic artificial synapse based on graphene/MoS 2 heterostructure, Sci. Adv. 7 (2021) 1–9, https://doi.org/10.1126/sciadv.abd9117.

[47] S. Zhang, L. Yang, C. Jiang, L. Sun, K. Guo, H. Han, W. Xu, Digitally aligned ZnO nanowire array based synaptic transistors with intrinsically controlled plasticity for short-term computation and long-term memory, Nanoscale 13 (2021) 19190–19199, https://doi.org/10.1039/d1nr04156h.

[48] X. Li, B. Yu, B. Wang, L. Bao, B. Zhang, H. Li, Z. Yu, T. Zhang, Y. Yang, R. Huang, Y. Wu, M. Li, Multi-terminal ionic-gated low-power silicon nanowire synaptic transistors with dendritic functions for neuromorphic systems, Nanoscale 12 (2020) 16348–16358, https://doi.org/10.1039/d0nr03141k.

[49] H. Wei, Z. Xu, Y. Ni, L. Yang, L. Sun, J. Gong, S. Zhang, S. Qu, W. Xu, Mixed-dimensional nanoparticle-nanowire channels for flexible optoelectronic artificial synapse with enhanced photoelectric response and asymmetric bidirectional plasticity, Nano Lett. 23 (2023) 8743–8752, https://doi.org/10.1021/acs.nanolett.3c02836.

[50] W. Huh, D. Lee, C.H. Lee, Memristors based on 2D materials as an artificial synapse for neuromorphic electronics, Adv. Mater. 32 (2020) 1–16, https://doi.org/10.1002/adma.202002092.

[51] F. Wang, F. Hu, M. Dai, S. Zhu, F. Sun, R. Duan, C. Wang, J. Han, W. Deng, W. Chen, M. Ye, S. Han, B. Qiang, Y. Jin, Y. Chua, N. Chi, S. Yu, D. Nam, S. H. Chae, Z. Liu, Q.J. Wang, A two-dimensional mid-infrared optoelectronic retina enabling simultaneous perception and encoding, Nat. Commun. 14 (2023) 1–8, https://doi.org/10.1038/s41467-023-37623-5.

[52] A.A. Talin, Y. Li, D.A. Robinson, E.J. Fuller, S. Kumar, ECRAM materials, devices, circuits and architectures: a perspective, Adv. Mater. 35 (2023) 1–21, https://doi.org/10.1002/adma.202204771.

[53] M. Huang, M. Schwacke, M. Onen, J. del Alamo, J. Li, B. Yildiz, Electrochemical ionic synapses: progress and perspectives, Adv. Mater. (2023) 35, https://doi.org/10.1002/adma.202205169.

[54] T.C. Südhof, Towards an understanding of synapse formation, Neuron 100 (2018) 276–293.

[55] D. Choquet, A. Triller, The dynamic synapse, Neuron 80 (2013) 691–703.

[56] A. Citri, R.C. Malenka, Synaptic plasticity: multiple forms, functions, and mechanisms, Neuropsychopharmacology 33 (2008) 18–41, https://doi.org/10.1038/sj.npp.1301559.

[57] M.F. Bear, L.N. Cooper, F.F. Ebner, A physiological basis for a theory of synapse modification, Science 237 (1987) 42–48 (80-.).

[58] R.S. Zucker, W.G. Regehr, Short-Term Synaptic Plasticity, Annu. Rev. Physiol. 64 (2002) 355–405.

[59] E.J. Nestler, Molecular basis of long-term plasticity underlying addiction, Nat. Rev. Neurosci. 2 (2001) 119–128.

[60] A. Basu, J. Acharya, T. Karnik, H. Liu, H. Li, J.S. Seo, C. Song, Low-power, adaptive neuromorphic systems: recent progress and future directions, IEEE J. Emerg. Sel. Top. Circuits Syst. 8 (2018) 6–27.

[61] B. Rajendran, A. Sebastian, M. Schmuker, N. Srinivasa, E. Eleftheriou, Low-power neuromorphic hardware for signal processing applications: a review of architectural and system-level design approaches, IEEE Signal Process. Mag. 36 (2019) 97–110.

[62] N. Makivić, K.D. Harris, J.M. Tarascon, B. Limoges, V. Balland, Impact of reversible proton insertion on the electrochemistry of electrode materials operating in mild aqueous electrolytes: a case study with TiO2, Adv. Energy Mater. 13 (2023), https://doi.org/10.1002/aenm.202203122.

[63] R. Dronskowski, Classical Approaches, in: Comput. Chem. Solid State Mater., Wiley, 2005, pp. 7–43, https://doi.org/10.1002/9783527612277.

[64] Y. van de Burgt, E. Lubberman, E.J. Fuller, S.T. Keene, G.C. Faria, S. Agarwal, M. J. Marinella, A. Alec Talin, A. Salleo, A non-volatile organic electrochemical device as a low-voltage artificial synapse for neuromorphic computing, Nat. Mater. 16 (2017) 414–418, https://doi.org/10.1038/nmat4856.

[65] Y.Y. Zhao, W.J. Sun, J. Wang, J.H. He, H. Li, Q.F. Xu, N.J. Li, D.Y. Chen, J.M. Lu, All-Inorganic Ionic Polymer-Based Memristor for High-Performance and Flexible Artificial Synapse, Adv. Funct. Mater. 30 (2020) 2004245, https://doi.org/10.1002/adfm.202004245.

[66] X. Yao, K. Klyukin, W. Lu, M. Onen, S. Ryu, D. Kim, N. Emond, I. Waluyo, A. Hunt, J.A. del Alamo, J. Li, B. Yildiz, Protonic solid-state electrochemical synapse for physical neural networks, Nat. Commun. 11 (2020) 3134, https://doi.org/10.1038/s41467-020-16866-6.

[67] S. Thakoor, A. Moopenn, T. Daud, A.P. Thakoor, Solid-state thin-film memistor for electronic neural networks, J. Appl. Phys. 67 (1990) 3132–3135, https://doi.org/10.1063/1.345390.

[68] Y. Van De Burgt, E. Lubberman, E.J. Fuller, S.T. Keene, G.C. Faria, S. Agarwal, M. J. Marinella, A. Alec Talin, A. Salleo, A non-volatile organic electrochemical device as a low-voltage artificial synapse for neuromorphic computing, Nat. Mater. 16 (2017) 414–418, https://doi.org/10.1038/NMAT4856.

[69] R.S. Vemuri, M.H. Engelhard, C.V. Ramana, Correlation between surface chemistry, density, and band gap in nanocrystalline WO 3 thin films, ACS Appl. Mater. Interfaces 4 (2012) 1371–1377, https://doi.org/10.1021/am2016409.

[70] M. Onen, N. Emond, J. Li, B. Yildiz, J.A. del Alamo, CMOS-compatible protonic programmable resistor based on phosphosilicate glass electrolyte for analog deep learning, Nano Lett. 21 (2021) 6111–6116, https://doi.org/10.1021/acs.nanolett.1c01614.

[71] A. Melianas, T.J. Quill, G. LeCroy, Y. Tuchman, H.V. Loo, S.T. Keene, A. Giovannitti, H.R. Lee, I.P. Maria, I. McCulloch, A. Salleo, Temperature-resilient solid-state organic artificial synapses for neuromorphic computing, Sci. Adv. 6 (2020) 1–8, https://doi.org/10.1126/sciadv.abb2958.

[72] T. Katase, T. Onozato, M. Hirono, T. Mizuno, H. Ohta, A transparent electrochromic metal-insulator switching device with three-terminal transistor geometry, Sci. Rep. 6 (2016) 1–9, https://doi.org/10.1038/srep25819.

[73] C. Oh, M. Jo, J. Son, All-solid-state synaptic transistors with high-temperature stability using proton pump gating of strongly correlated materials, ACS Appl. Mater. Interfaces. 11 (2019) 15733–15740, https://doi.org/10.1021/acsami.9b00392.

[74] R.D. Nikam, J. Lee, W. Choi, W. Banerjee, M. Kwak, M. Yadav, H. Hwang, Ionic sieving through one-atom-thick 2D material enables analog nonvolatile memory for neuromorphic computing, Small. 17 (2021) 2103543, https://doi.org/10.1002/smll.202103543.

[75] A. Melianas, M.A. Kang, A. VahidMohammadi, T.J. Quill, W. Tian, Y. Gogotsi, A. Salleo, M.M. Hamedi, High-speed ionic synaptic memory based on 2D titanium carbide MXene, Adv. Funct. Mater. 32 (2022) 2109970, https://doi.org/10.1002/adfm.202109970.

[76] Y. Li, J. Lu, D. Shang, Q. Liu, S. Wu, Z. Wu, X. Zhang, J. Yang, Z. Wang, H. Lv, M. Liu, Oxide-based electrolyte-gated transistors for spatiotemporal information processing, Adv. Mater. 32 (2020) 1–12, https://doi.org/10.1002/adma.202003018.

[77] J. Tang, D. Bishop, S. Kim, M. Copel, T. Gokmen, T. Todorov, S. Shin, K.T. Lee, P. Solomon, K. Chan, W. Haensch, J. Rozen, ECRAM as scalable synaptic cell for high-speed, low-power neuromorphic computing, in: 2018 IEEE Int. Electron Devices Meet, IEEE, 2018, https://doi.org/10.1109/IEDM.2018.8614551, 13.1.1-13.1.4.

[78] R.D. Nikam, M. Kwak, J. Lee, K.G. Rajput, W. Banerjee, H. Hwang, Near ideal synaptic functionalities in Li ion synaptic transistor using Li3POxSex electrolyte with high ionic conductivity, Sci. Rep. 9 (2019) 1–11, https://doi.org/10.1038/s41598-019-55310-8.

[79] M. Nakayama, M. Kaneko, M. Wakihara, First-principles study of lithium ion migration in lithium transition metal oxides with spinel structure, Phys. Chem. Chem. Phys. 14 (2012) 13963–13970.

[80] M.J. Choi, J.H. Baek, J.Y. Kim, H.W. Jang, Highly textured and crystalline materials for rechargeable Li-ion batteries, Batter. Energy. 2 (2023) 20230010, https://doi.org/10.1002/bte2.20230010.

[81] C. Li, B. Liu, N. Jiang, Y. Ding, Elucidating the charge-transfer and Li-ion-migration mechanisms in commercial lithium-ion batteries with advanced electron microscopy, Nano Res. Energy. 1 (2022) e9120031.

[82] J.A. Gilbert, I.A. Shkrob, D.P. Abraham, Transition metal dissolution, ion migration, electrocatalytic reduction and capacity loss in lithium-ion full cells, J. Electrochem. Soc. 164 (2017) A389.

[83] C.S. Yang, D.S. Shang, N. Liu, E.J. Fuller, S. Agrawal, A.A. Talin, Y.Q. Li, B. G. Shen, Y. Sun, All-solid-state synaptic transistor with ultralow conductance for neuromorphic computing, Adv. Funct. Mater. 28 (2018) 1804170, https://doi.org/10.1002/adfm.201804170.

[84] M. Rajapakse, B. Karki, U.O. Abu, S. Pishgar, M.R.K. Musa, S.M.S. Riyadh, M. Yu, G. Sumanasekera, J.B. Jasinski, Intercalation as a versatile tool for fabrication, property tuning, and phase transitions in 2D materials, Npj 2D Mater. Appl. 5 (2021), https://doi.org/10.1038/s41699-021-00211-6.

[85] Y. Wu, D. Li, C.L. Wu, H.Y. Hwang, Y. Cui, Electrostatic gating and intercalation in 2D materials, Nat. Rev. Mater. 8 (2023) 41–53, https://doi.org/10.1038/s41578-022-00473-6.

[86] J. Zhu, Y. Yang, R. Jia, Z. Liang, W. Zhu, Z.U. Rehman, L. Bao, X. Zhang, Y. Cai, L. Song, R. Huang, Ion gated synaptic transistors based on 2D van der Waals crystals with tunable diffusive dynamics, Adv. Mater. 30 (2018) 1800195, https://doi.org/10.1002/adma.201800195.

[87] L. Bao, J. Zhu, Z. Yu, R. Jia, Q. Cai, Z. Wang, L. Xu, Y. Wu, Y. Yang, Y. Cai, R. Huang, Dual-gated MoS2 neuristor for neuromorphic computing, ACS Appl. Mater. Interfaces. 11 (2019) 41482–41489, https://doi.org/10.1021/acsami.9b10072.

[88] M.T. Sharbati, Y. Du, J. Torres, N.D. Ardolino, M. Yun, F. Xiong, Low-power, electrochemically tunable graphene synapses for neuromorphic computing, Adv. Mater. 30 (2018) 1802353, https://doi.org/10.1002/adma.201802353.

[89] Z. Wang, M. Rao, R. Midya, S. Joshi, H. Jiang, P. Lin, W. Song, S. Asapu, Y. Zhuo, C. Li, H. Wu, Q. Xia, J.J. Yang, Threshold switching of Ag or Cu in dielectrics: materials, mechanism, and applications, Adv. Funct. Mater. 28 (2018) 1704862, https://doi.org/10.1002/adfm.201704862.

[90] R. Midya, Z. Wang, J. Zhang, S.E. Savel'ev, C. Li, M. Rao, M.H. Jang, S. Joshi, H. Jiang, P. Lin, K. Norris, N. Ge, Q. Wu, M. Barnell, Z. Li, H.L. Xin, R.S. Williams, Q. Xia, J.J. Yang, Anatomy of Ag/Hafnia-based selectors with 1010 nonlinearity, Adv. Mater. 29 (2017) 1604457, https://doi.org/10.1002/adma.201604457.

[91] M. Zhao, B. Gao, J. Tang, H. Qian, H. Wu, Reliability of analog resistive switching memory for neuromorphic computing, Appl. Phys. Rev. 7 (2020) 011301, https://doi.org/10.1063/1.5124915.

[92] J.H. Baek, K.J. Kwak, S.J. Kim, J. Kim, J.Y. Kim, I.H. Im, S. Lee, K. Kang, H. W. Jang, Two-terminal lithium-mediated artificial synapses with enhanced weight modulation for feasible hardware neural networks, Nano-Micro Lett. 15 (2023) 69, https://doi.org/10.1007/s40820-023-01035-3.

[93] P. Gupta, S. Pushpakanth, M.A. Haider, S. Basu, Understanding the design of cathode materials for Na-ion batteries, ACS. Omega 7 (2022) 5605–5614, https://doi.org/10.1021/acsomega.1c05794.

[94] S.W. Kim, D.H. Seo, X. Ma, G. Ceder, K. Kang, Electrode materials for rechargeable sodium-ion batteries: potential alternatives to current lithium-ion batteries, Adv. Energy Mater. 2 (2012) 710–721, https://doi.org/10.1002/aenm.201200026.

[95] C.W. Lee, S.E. Jun, S.J. Kim, T.H. Lee, S.A. Lee, J.W. Yang, J.H. Cho, S. Choi, C. Kim, S.Y. Kim, H.W. Jang, Rationally designed graphene channels for real-time sodium ion detection for electronic tongue, InfoMat 5 (2023) e12427, https://doi.org/10.1002/inf2.12427.

[96] J. Park, Z.L. Xu, K. Kang, Solvated ion intercalation in graphite: sodium and beyond, Front. Chem. 8 (2020) 1–14, https://doi.org/10.3389/fchem.2020.00432.

[97] Z.L. Xu, G. Yoon, K.Y. Park, H. Park, O. Tamwattana, S. Joo Kim, W.M. Seong, K. Kang, Tailoring sodium intercalation in graphite for high energy and power sodium ion batteries, Nat. Commun. 10 (2019) 1–10, https://doi.org/10.1038/s41467-019-10551-z.

[98] A. Massaro, A. Pecoraro, A.B. Muñoz-García, M. Pavone, First-principles study of na intercalation and diffusion mechanisms at 2D MoS2/graphene interfaces, J. Phys. Chem. C. 125 (2021) 2276–2286, https://doi.org/10.1021/acs.jpcc.0c10107.

[99] Z.G. Liu, R. Du, X.X. He, J.C. Wang, Y. Qiao, L. Li, S.L. Chou, Recent progress on intercalation-based anode materials for low-cost sodium-ion batteries, ChemSusChem. 14 (2021) 3724–3743, https://doi.org/10.1002/cssc.202101186.

[100] B. Wang, X. Wang, E. Wang, C. Li, R. Peng, Y. Wu, Z. Xin, Y. Sun, J. Guo, S. Fan, C. Wang, J. Tang, K. Liu, Monolayer MoS2 synaptic transistors for high-temperature neuromorphic applications, Nano Lett. 21 (2021) 10400–10408, https://doi.org/10.1021/acs.nanolett.1c03684.

[101] L. Hu, L. Li, K.C. Chang, X. Lin, P. Huang, S. Zhang, Ultrasensitive freestanding and mechanically durable artificial synapse with attojoule power based on Na-salt doped polymer for biocompatible neuromorphic interface, Adv. Funct. Mater. 31 (2021) 2106015, https://doi.org/10.1002/adfm.202106015.

[102] W. Huh, S. Jang, J.Y. Lee, D. Lee, D. Lee, J.M. Lee, H.G. Park, J.C. Kim, H. Y. Jeong, G. Wang, C.H. Lee, Synaptic barristor based on phase-engineered 2D heterostructures, Adv. Mater. 30 (2018) 1–7, https://doi.org/10.1002/adma.201801447.

[103] J. Yin, F. Zeng, Q. Wan, F. Li, Y. Sun, Y. Hu, J. Liu, G. Li, F. Pan, Adaptive crystallite kinetics in homogenous bilayer oxide memristor for emulating diverse synaptic plasticity, Adv. Funct. Mater. 28 (2018) 1–10, https://doi.org/10.1002/adfm.201706927.

[104] X. Yan, C. Qin, C. Lu, J. Zhao, R. Zhao, D. Ren, Z. Zhou, H. Wang, J. Wang, L. Zhang, X. Li, Y. Pei, G. Wang, Q. Zhao, K. Wang, Z. Xiao, H. Li, Robust Ag/ZrO2/WS2/Pt memristor for neuromorphic computing, ACS Appl. Mater. Interfaces 11 (2019) 48029–48038, https://doi.org/10.1021/acsami.9b17160.

[105] R. Xu, H. Jang, M.H. Lee, D. Amanov, Y. Cho, H. Kim, S. Park, H.J. Shin, D. Ham, Vertical MoS 2 double-layer memristor with electrochemical metallization as an atomic-scale synapse with switching thresholds approaching 100mV, Nano Lett. 19 (2019) 2411–2417, https://doi.org/10.1021/acs.nanolett.8b05140.

[106] M. Fitzgerald, The development of nociceptive circuits, Nat. Rev. Neurosci. 6 (2005) 507–520, https://doi.org/10.1038/nrn1701.

[107] H.W. Tao, M.M. Poo, Activity-dependent matching of excitatory and inhibitory inputs during refinement of visual receptive fields, Neuron 45 (2005) 829–836, https://doi.org/10.1016/j.neuron.2005.01.046.

[108] M. Fitzgerald, Spontaneous and evoked activity of fetal primary afferents in vivo, Nature 326 (1987) 603–605, https://doi.org/10.1038/326603a0.

[109] M. Galarreta, S. Hestrin, Electrical and chemical synapses among parvalbumin fast-spiking GABAergic interneurons in adult mouse neocortex, Proc. Natl. Acad. Sci. U. S. A. 99 (2002) 12438–12443, https://doi.org/10.1073/pnas.192159599.

[110] M. Galarreta, S. Hestrin, What cell types form electrical synapses? Nat. Rev. Neurosci. 2 (2001). www.nature.com/reviews/neuro.

[111] K. Lee, J. Lee, R.D. Nikam, S. Heo, H. Hwang, Sodium-based nano-ionic synaptic transistor with improved retention characteristics, Nanotechnology. 31 (2020) 455204, https://doi.org/10.1088/1361-6528/abaa0e.
[112] K.C. Kwon, J.H. Baek, K. Hong, S.Y. Kim, H.W. Jang, Correction to: memristive devices based on two-dimensional transition metal chalcogenides for neuromorphic computing, Nano-Micro Lett. 14 (1) (2022) 1–3, https://doi.org/10.1007/s40820-022-00816-6 (58)10.1007/s40820-021-00784-3, Nano-Micro Lett. 14 (2022).
[113] E.K. Jang, Y. Park, J.S. Lee, Reversible uptake and release of sodium ions in layered SnS2-reduced graphene oxide composites for neuromorphic devices, Nanoscale 11 (2019) 15382–15388, https://doi.org/10.1039/C9NR03073E.
[114] J. Malinsky, M. Opekarová, New insight into the roles of membrane microdomains in physiological activities of fungal cells, in: 2016: pp. 119–180. https://doi.org/10.1016/bs.ircmb.2016.02.005.
[115] A.A. Ramahi, R.L. Ruff, Membrane Potential, in: Encycl. Neurol. Sci., Elsevier, 2014, pp. 1034–1035, https://doi.org/10.1016/B978-0-12-385157-4.00062-2.
[116] Y. Cao, T. Zhao, C. Zhao, Y. Liu, P. Song, H. Gao, C.Z. Zhao, Advanced artificial synaptic thin-film transistor based on doped potassium ions for neuromorphic computing via third-generation neural network, J. Mater. Chem. C. 10 (2022) 3196–3206, https://doi.org/10.1039/D1TC04827A.
[117] Y. Li, T.P. Xiao, C.H. Bennett, E. Isele, A. Melianas, H. Tao, M.J. Marinella, A. Salleo, E.J. Fuller, A.A. Talin, In situ parallel training of analog neural network using electrochemical random-access memory, Front. Neurosci. 15 (2021) 1–14, https://doi.org/10.3389/fnins.2021.636127.